NUCLEAR DATA AND MEASUREMENTS SERIES

ANL/NDM-119

Fast-Neutron Interaction with Elemental Zirconium, and the Dispersive Optical Model

by

S. Chiba, P.T. Guenther, A.B. Smith, M. Sugimoto, and R.D. Lawson

June 1991

ARGONNE NATIONAL LABORATORY,
ARGONNE, ILLINOIS 60439, U.S.A.

NUCLEAR DATA AND MEASUREMENTS SERIES

ANL/NDM–119

FAST–NEUTRON INTERACTION
WITH ELEMENTAL ZIRCONIUM,
AND THE DISPERSIVE OPTICAL MODEL

S. Chiba, P. T. Guenther, A. B. Smith, M. Sugimoto,
and R. D. Lawson
June 1991

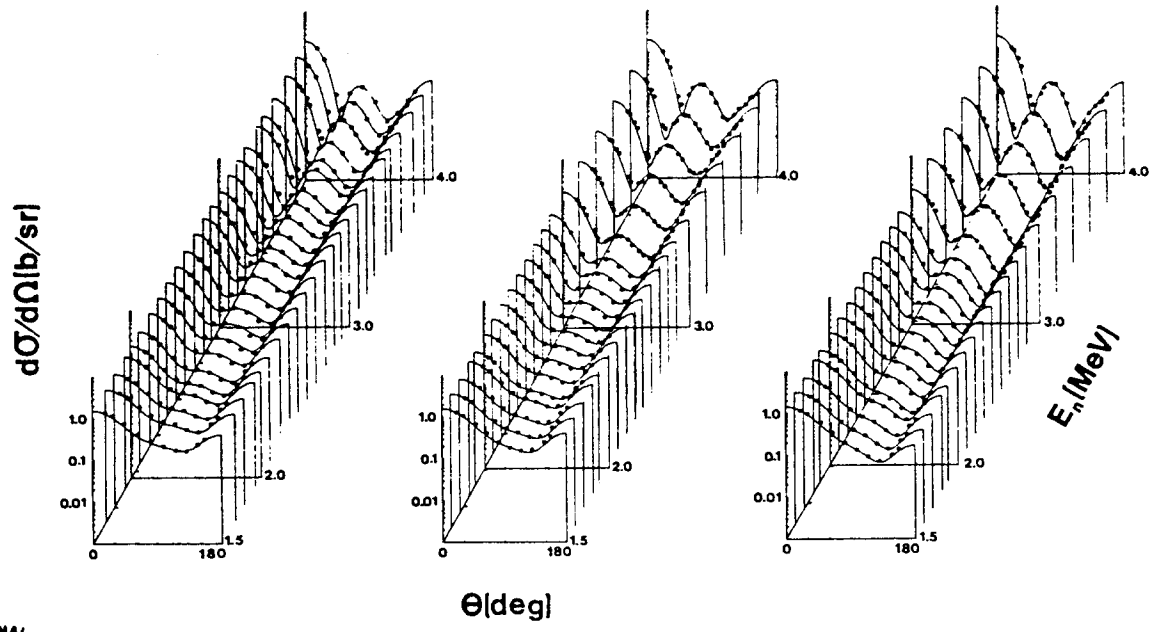

ARGONNE NATIONAL LABORATORY, ARGONNE, ILLINOIS

Operated by THE UNIVERSITY OF CHICAGO
for the U. S. DEPARTMENT OF ENERGY
under Contract W-31-109-Eng-38

Argonne National Laboratory, with facilities in the states of Illinois and Idaho, is owned by the United States government, and operated by The University of Chicago under the provisions of a contract with the Department of Energy.

Reproduced from the best available copy.

Available to DOE and DOE contractors from the
Office of Scientific and Technical Information
P.O. Box 62
Oak Ridge, TN 37831
Prices available from (615) 576-8401, FTS 626-8401

Available to the public from the
National Technical Information Service
U.S. Department of Commerce
5285 Port Royal Road
Springfield, VA 22161

ANL/NDM–119

FAST–NEUTRON INTERACTION WITH ELEMENTAL ZIRCONIUM, AND THE DISPERSIVE OPTICAL MODEL*

by

S. Chiba+, P. T. Guenther, A. B. Smith, M. Sugimoto+, and R. D. Lawson

June 1991

Keywords

Measured σ_{el} and σ_{inel} of elemental Zr for neutrons of 1.5 – 10 MeV. Optical–statistical model interpretation and the dispersion relationship.

Engineering Physics Division
ARGONNE NATIONAL LABORATORY
9700 South Cass Avenue
Argonne, Illinois 60439
U. S. A.

*This work supported by the U.S. Department of Energy under contract No. W–31–109–Eng–38.

+Visiting scientist from Japan Atomic Energy Research Institute, Tokai Establishment.

NUCLEAR DATA AND MEASUREMENTS SERIES

The Nuclear Data and Measurements Series presents results of studies in the field of microscopic nuclear data. The primary objective is the dissemination of information in the comprehensive form required for nuclear technology applications. This Series is devoted to: a) measured microscopic nuclear parameters, b) experimental techniques and facilities employed in measurements, c) the analysis, correlation and interpretation of nuclear data, and d) the evaluation of nuclear data. Contributions to this Series are reviewed to assure technical competence and, unless otherwise stated, the contents can be formally referenced. This Series does not supplant formal journal publication, but it does provide the more extensive information required for technological applications (e.g., tabulated numerical data) in a timely manner.

TABLE OF CONTENTS

INFORMATION ABOUT OTHER ISSUES OF THE ANL/NDM SERIES

A list of titles and authors for all the previous issues appears in each report of the series. The list for reports ANL/NDM–1 through ANL/NDM–75 appears in ANL/NDM–76, and ANL/NDM–91 contains the list for reports ANL/NDM–76 through ANL/NDM–90. Below is the list for ANL/NDM–91 up to the current report. Requests for a complete list of titles or for copies of previous reports should be directed to:

Section Secretary
Applied Nuclear Physics Section
Engineering Physics Division
Building 316
Argonne National Laboratory
9700 South Cass Avenue
Argonne, Illinois 60439
U.S.A.

ANL/NDM–91 A.B. Smith, P.T. Guenther and R.D. Lawson, *On the Energy Dependence of the Optical Model of Neutron Scattering from Niobium*, May 1985.

ANL/NDM–92 Donald L. Smith, *Nuclear Data Uncertainties (Vol.–I): Basic Concepts of Probability*, December 1988.

ANL/NDM–93 D.L. Smith, J.W. Meadows and M.M. Bretscher, *Integral Cross–section Measurements for* $^{7}Li(n,n't)^{4}He$, $^{27}Al(n,p)^{27}Mg$, $^{27}Al(n,\alpha)^{24}Na$, $^{58}Ni(n,p)^{58}Co$, *and* $^{60}Ni(n,p)^{60}Co$ *Relative to* ^{238}U *Neutron Fission in the Thick–target* $^{9}Be(d,n)^{10}B$ *Spectrum at* $E_d = 7$ *MeV*, October 1985.

ANL/NDM–94 A.B. Smith, D.L. Smith, P. Rousset, R.D. Lawson and R.J. Howerton, *Evaluated Neutronic Data File for Yttrium*, January 1986.

ANL/NDM–95 Donald L. Smith and James W. Meadows, *A Facility for High–intensity Neutron Irradiations Using Thick–target Sources at the Argonne Fast–neutron Generator*, May 1986.

ANL/NDM–96 M. Sugimoto, A.B. Smith and P.T. Guenther, *Ratio of the Prompt–fission–neutron Spectrum of Plutonium–239 to that of Uranium–235*, September 1986.

ANL/NDM–97 J.W. Meadows, *The Fission Cross Sections of* ^{230}Th, ^{232}Th, ^{233}U, ^{234}U, ^{236}U, ^{238}U, ^{237}Np, ^{239}Pu, *and* ^{242}Pu *Relative* ^{235}U *at 14.74 MeV Neutron Energy*, December 1986.

ANL/NDM–98 J.W. Meadows, *The Fission Cross Section Ratios and Error Analysis for Ten Thorium, Uranium, Neptunium and Plutonium Isotopes at 14.74–MeV Neutron Energy*, March 1987.

ANL/NDM–99 Donald L. Smith, *Some Comments on the Effects of Long–range Correlations in Covariance Matrices for Nuclear Data*, March 1987.

ANL/NDM–100 A.B. Smith, P.T. Guenther and R.D. Lawson, *The Energy Dependence of the Optical–model Potential for Fast–neutron Scattering from Bismuth*, May 1987.

ANL/NDM–101 A.B. Smith, P.T. Guenther, J.F. Whalen and R.D. Lawson, *Cobalt: Fast Neutrons and Physical Models*, July 1987.

ANL/NDM–102 D. L Smith, *Investigation of the Influence of the Neutron Spectrum in Determinations of Integral Neutron Cross–Section Ratios*, November 1987.

ANL/NDM–103 A.B. Smith, P.T. Guenther and B. Micklich, *Spectrum of Neutrons Emitted From a Thick Beryllium Target Bombarded With 7 MeV Deuterons*, January 1988.

ANL/NDM–104 L.P. Geraldo and D.L. Smith, *Some Thoughts on Positive Definiteness in the Consideration of Nuclear Data Covariance Matrices*, January 1988.

ANL/NDM–105 A.B. Smith, D.L. Smith, P.T. Guenther, J.W. Meadows, R.D. Lawson, R.J. Howerton, and T. Djemil, *Neutronic Evaluated Nuclear–Data File for Vanadium*, May 1988.

ANL/NDM–106 A.B. Smith, P.T. Guenther, and R.D. Lawson, *Fast–Neutron Elastic Scattering from Elemental Vanadium*, March 1988.

ANL/NDM–107 P. Guenther, R. Lawson, J. Meadows, M. Sugimoto, A. Smith, D. Smith, and R. Howerton, *An Evaluated Neutronic Data File for Elemental Cobalt*, August 1988.

ANL/NDM–108 M. Sugimoto, P.T. Guenther, J.E. Lynn, A.B. Smith, and J.F. Whalen, *Some Comments on the Interaction of Fast–Neutrons with Beryllium*, November 1988.

ANL/NDM–109 P.T. Guenther, R.D. Lawson, J.W. Meadows, A.B. Smith, D.L. Smith, and M. Sugimoto, *An Evaluated Neutronic Data File for Bismuth*, November 1989.

ANL/NDM–110 D.L. Smith and L.P. Geraldo, *A Vector Model for Error Propagation*, March 1989.

ANL/NDM–111 J.E. Lynn, *Fifty Years of Nuclear Fission*, June 1989.

ANL/NDM–112 S. Chiba, P.T. Guenther, and A.B. Smith, *Some Remarks on the Neutron Elastic– and Inelastic–Scattering Cross Sections of Palladium*, May 1989.

ANL/NDM–113 J.E. Lynn, *Resonance Effects in Neutron Scattering Lengths*, June 1989.

ANL/NDM–114 A.B. Smith, R.D. Lawson, and P.T. Guenther, *Ambiguities in the Elastic Scattering of 8 MeV Neutrons from Adjacent Nuclei*, October 1989.

ANL/NDM–115 A.B. Smith, S. Chiba, D.L. Smith, J.W. Meadows, P.T. Guenther, R.D. Lawson, and R.J. Howerton, *Evaluated Neutronic File for Indium*, January 1990.

ANL/NDM–116 S. Chiba, P.T. Guenther, R.D. Lawson, and A.B. Smith, *Neutron Scattering from Elemental Indium, the Optical Model, and the Bound–State Potential*, June 1990.

ANL/NDM–117 Donald L. Smith and Luiz P. Geraldo, *An Evaluation of the Nb–93(n,n')Nb–93m Dosimeter Reaction for ENDF/B–VI*, November 1990.

ANL/NDM–118 J.W. Meadows, *Characteristics of the Samples in the FNG Fission Deposit Collection*, December 1990.

FAST–NEUTRON INTERACTION WITH ELEMENTAL ZIRCONIUM, AND THE DISPERSIVE OPTICAL MODEL

S. Chiba, P. T. Guenther, A. B. Smith,
M. Sugimoto, and R. D. Lawson

ABSTRACT

Differential neutron elastic– and inelastic–scattering cross sections of elemental zirconium are measured from ≈ 1.5 to 10 MeV. Below 3 MeV the measurements are made at incident-neutron energy intervals of ≈ 100 keV, from 3 to 4 MeV at intervals of ≈ 200 keV, and at intervals of ≈ 500 keV at higher energies. The angular range of the measurements is ≈ 18° to 160°, with up to more than 100 differential values per distribution. This comprehensive data base, augmented with a 24–MeV elastic–scattering distribution from the literature, is used to develop two phenomenological optical–statistical models which both describe the data very well. First, the parameters of the conventional spherical optical model (SOM) are deduced. Secondly, the model in which the change in the real potential brought about by the dispersion relationship (DOM) is examined. The SOM parameters are consistent with systematics previously reported from this laboratory, and the volume–integral-per-nucleon of the real potential strength, J_v, and the radius, r_v, are energy dependent. When the DOM is used, a substantial part of the energy dependence of J_v (≈ 30%) disappears. However, the change in the energy dependence of r_v is small, so that a significant energy dependence remains when the DOM is used. Both models are extrapolated to the bound-state regime where they have modest success in predicting the binding energies of the single–particle and single–hole states in ^{90}Zr.

I. INTRODUCTION

The total and elastic–scattering cross sections of fast neutrons from nuclei are generally described in terms of an optical model having real, imaginary and spin–orbit components. For spherical nuclei there are two variants of this model in vogue at present. In the first (hereafter referred to as the spherical optical model, SOM), the real potential is taken to have the Woods–Saxon shape, the imaginary potential the surface–peaked derivative of the Woods–Saxon well, with perhaps a volume absorption setting in at energies of $\approx > 20$ MeV, and a spin–orbit potential of the Thomas form.[1] In the second formulation, the fundamental dispersion relationship,[2] which links the real and imaginary optical–model potentials, is taken into account, and this will be referred to as the dispersive optical model (DOM). In this paper, parameters which define both an SOM and a DOM describing neutron scattering from elemental zirconium are deduced. The applied importance of a reliable model for elemental zirconium is clear, since zirconium is a key component of fissile alloys used in the most promising, and inherently safe, fast fission-reactor concept (the Integral Fast Reactor, IFR).[3] To apply the elemental zirconium model to specific isotopes, one must know the magnitude and sign of the Lane term of the potentials,[4] that is, the $(N-Z)/A$ term. This, of course, cannot be determined from our elemental data, but it can be deduced from the Ohio University studies[5,6] which involve separated zirconium isotopes. It should be noted that the coefficient of the $(N-Z)/A$ term extracted from the Ohio data has the opposite sign for the imaginary potential relative to that given by global models.[7,8] The sign is, however, consistent with the results of 8 MeV ratio measurements made at this laboratory,[9] and with the fact that the imaginary potential increases rapidly as one moves away from a closed shell.[10]

Since we consider the differential elastic–scattering cross sections between ≈ 1.5 and 24 MeV and total cross sections from thermal to 20 MeV, the energy variation of the model parameters is reasonably well–defined over a wide range. As both the SOM and the DOM are fitted to the same data, we can check the conjecture[11] that the energy dependence of the geometric parameters of the real SOM are due entirely to the fact that the dispersion contribution to the real potential was neglected. Furthermore, as discussed by Mahaux and collaborators,[12,13,14] once the energy variation of the optical–model parameters is known, one can use the dispersion relationship to extrapolate to the bound–state regime; that is, deduce the shell–model potential. Thus, combining this with the $(N-Z)/A$ dependence discussed above, one can examine the neutron binding energies of the single-particle and single–hole states of the closed shell nucleus ^{90}Zr.

In Section II, the experimental procedures used in the present measurements are outlined. In Section III, the experimental results are presented. Sections IV and V are devoted to the determination of the parameters of the SOM and the DOM, respectively, and to comparing the theoretical predictions, made on the basis of these models, with the experimental results. The predicted binding energies of the neutron single–particle and single–hole states in ^{90}Zr are discussed for both the SOM and the DOM in Section VI. Finally, in Section VII our results are summarized and discussed.

II. EXPERIMENTAL PROCEDURES

All of the measurements were made using the pulsed–beam fast–neutron time–of–flight technique. The neutron angular distributions were determined using the Argonne 10–angle time–of–flight apparatus.[15,16] Higher–resolution measurements were made at selected energies using a heavily shielded 14.52 m flight path at a scattering angle of 80°.[17]

The scattering samples were solid metal cylinders of elemental zirconium 2 cm in diameter and 2 cm long. The chemical purity of the samples was > 99%. Below 4 MeV, reference standard samples of carbon (pile grade graphite) were used, and above 4 MeV, the reference standard was hydrogen in the form of polyethylene (CH_2). The standard samples were the same dimensions as the zirconium ones, with chemical purity of better than 99%. The weights of all the samples were measured to an accuracy of better than 0.01% using conventional techniques. The samples were believed to be of uniform density, although the measurements were not sensitive to this uniformity.

Two types of neutron sources were employed in the measurements. Below 4 MeV, the ^{7}Li(p,n) reaction[18] was used, with the lithium metal vacuum evaporated onto tantalum backings to thicknesses giving neutron energy spreads of ≈ 50 keV at a 0° source–reaction angle. Above 4 MeV, the D(d,n) reaction[18] was used, with the deuterium gas contained in a cell ≈ 2 cm long. The deuterium gas pressure within the cell was adjusted to give neutron energy spreads at a 0° source–reaction angle of ≈ 250 keV at 4.5 MeV and decreasing to ≈ 125 keV at 10 MeV. The mean energy of the neutron sources was determined to ≈ ≤ 20 keV by magnetic analysis of the incident charged–particle beam. The neutron sources were pulsed at a repetition rate of 2 MHz, with a burst duration of ≈ 1 nsec. Source intensities were enhanced through the use of a harmonic ion–beam bunching system.

The scattering samples were placed ≈ 17 cm from the neutron source at a 0° reaction angle. In the angular–distribution measurements, a massive collimator system defined the ten flight paths of ≈ 500 cm, distributed over scattering angles between 18° and 160°. The relative angular scale of the scattering apparatus was determined to ≈ 0.1° using optical instruments. Below an incident energy of 4 MeV, the zero of this angular scale was determined to ≈ 0.2° using optical methods. This degree of accuracy was believed to be sufficient at lower energies where the scattered–neutron distributions are not violently forward peaked. Above 4 MeV, the zero for the angular scale was determined to better than 0.15° by the observation of neutrons scattered from a relatively heavy target (usually niobium) both right and left of the apparent center line, over a forward angular range where the elastic–scattering from the sample is very rapidly changing with angle. One or more additional time–of–flight detectors were placed at a source–reaction angle of ≈ 5°, in order to monitor source intensity. These monitors were supported by conventional long-counters. In the higher–resolution, long flight–path measurements, the neutron source and sample were surrounded by a massive concrete shield approximately 1.5 m thick. The interior of this shield was a room approximately 2.5 m on a side, lined with polyethylene, cadmium, and boron in order to reduce backscattering to the sample position. A precision collimator penetrated this shielded vault at an 80° scattering angle.

The neutron detectors used in the angular–distribution measurements were organic liquid scintillators,[19] 2 cm thick and 12.5 cm in diameter. Their γ–ray response was

suppressed using pulse–shape–discrimination techniques. Similar scintillators were used for the long–flight–path, higher–resolution measurements, but they were larger (5 cm in thickness and 25 cm in diameter), and four of them were arranged in a square array. This array was placed within a concrete shield approximately 1 m thick, in order to suppress the ambient background. The relative energy dependencies of the detectors were determined by the observation of neutrons emitted in the spontaneous fission of ^{252}Cf, as described in Ref. 20. These relative sensitivities were normalized to either hydrogen or carbon reference standards[21] by observing either differential elastic scattering from polyethylene (for measurements > 4 MeV) or the total cross section of carbon as described in Ref. 22 (for measurements < 4 MeV). As a practical convenience, in the long flight–path measurements an intermediate secondary reference was used, either the elastic scattering from zirconium or the cross section for the inelastic excitation of the 1.454 MeV (2^+) level of ^{58}Ni, both as determined in the short flight–path measurements.

The incoming experimental information was sorted and stored in a digital computer, and then reduced to cross sections using a complex data–processing system that has been developed over many years.[23] A part of this system included Monte–Carlo corrections for multiple–event, angular–resolution and beam–attenuation effects.[24] The Monte–Carlo procedures were pursued through three iterations, to assure a level of convergence which provided accuracies of approximately 1%.

III. EXPERIMENTAL RESULTS

A. Elastic Neutron Scattering

At few–MeV energies, the elastic–scattering cross sections of zirconium may fluctuate with energy due to residual resonance effects. Therefore, at energies below 4 MeV the elastic–scattering measurements were undertaken in considerable energy detail with 50–70 keV incident–neutron energy spreads. The scattered–neutron resolution was sufficient to separate the elastic component from the inelastic contributions. The angular distributions were measured at ≈ 70–100 keV intervals from ≈ 1.5 to 3.0 MeV. At these lower energies and broad incident resolutions, the observed angular distributions do not display a great deal of structure. So, they were reasonably well–defined by ten differential measurements at each incident energy, distributed between ≈ 25° and 155°. From 3 to 4 MeV, the elastic–scattering distributions were measured at ≈ 200–keV incident–energy intervals, with 20 differential values per distribution. The total uncertainties in the individual differential values (including counting statistics, angular uncertainties, correction factors, and normalizations) were estimated to be ≤ 5%. These lower–energy results were obtained at this laboratory some time ago, and are discussed in more detail in Ref. 25.

Above 4 MeV, the measurements were made at approximately 0.5–MeV intervals from 4.5 to 10.0 MeV, and the angular range was approximately 18° to 160°. The data were taken over several years, in sets of 20–40 angular values at each measurement period and incident energy. When combined, the average number of differential values per distribution was 107, sufficient to give good definition of the angle–dependent structure. Throughout these measurements, the scattered–neutron resolution was sufficient to reasonably resolve the elastic– and inelastic–scattered contribution. In a number of ways (e.g., angular scale, detector normalizations, etc.), the measurements at the various

experimental periods were independent — thus reproducibility is some indicator of reliability. However, in other aspects (e.g., reference standard, correction procedures, etc.), the individually measured sets have the possibility of a common systematic uncertainty. The uncertainties associated with the differential values varied a great deal, depending on the care given a particular measurement and on the scattering angle. Except at the very minima of the distributions, statistical uncertainties were relatively small ($\lesssim 1\% - 3\%$), as were those associated with the Monte–Carlo correction procedures ($\lesssim 1\%$). The reference H(n,n) scattering standard is known to better than 1%. Although reproducibility of a number of measurements is some indication of angular uncertainty, this can be a serious problem where the cross sections are changing very rapidly with angle. The detector calibration procedures were complex, and it is difficult to quantify the uncertainties associated with them. A subjective estimate is $\approx< 3\%$ below 8 MeV, and $< 5\%$ at higher energies. It is likely that the major contributions to the uncertainties (e.g., detector calibrations, etc.) are systematic and correlated to some unknown extent. This possibility was ignored in the subsequent fitting procedures discussed in Section IV.

The elastic–scattering results described here are illustrated in Fig. III–1. Some isotopic elastic scattering results have been reported, and these will be compared with the present measurements in Section IV.

B. Inelastic Neutron Scattering

At lower energies the broad resolution required for a reasonable averaging of fluctuations in the elastic scattering precludes optimum resolution of the inelastically-scattered neutron groups. Moreover, elemental zirconium consists of four isotopes with significant abundance, resulting in a large elemental level density and, thus, very complex inelastically–scattered neutron spectra. Despite this, the discrete inelastic–scattering cross sections generally were determined for incident energies of less than 4 MeV. These results largely consisted of the composite contributions from the excitation of levels in several isotopes. Nine such "elemental" inelastic groups were identified and attributed to the excited levels given in Table III–1. The corresponding angle–integrated inelastic-scattering cross sections of the first five of these groups, shown in Fig. III–2, were obtained by fitting the measured differential cross sections with second–order Legendre–polynomial expansions. The illustrated uncertainties are larger than for elastic scattering, due to lower counting rates and to uncertainties in the experimental resolution of the underlying complex structures. There are remarkably few previously reported discrete inelastic-scattering cross sections of elemental zirconium, probably because of the experimental difficulties outlined above. There have been some isotopic results reported, and these are discussed and compared with the present study in Section IV.

Above 4 MeV incident–neutron energy, the inelastically–scattered neutron spectrum blends into a continuum upon which is superimposed some small structure, due to clumping of neutron groups from levels in the various isotopes. Spectra obtained with the 5 m flight paths displayed only a trace of the excitation of the 941 keV "group" observed at lower energies. This contribution was generally a very small artifact on the shoulder of the much larger elastic–scattering peak. Therefore, no attempt was made to deduce the corresponding cross sections from the 5 m measurements. There were two prominent structures in the spectra obtained at 5 m, one corresponding to excitations of $\approx$ 1.85–2.2 MeV, and the other to excitations of $\approx$ 2.6–2.9 MeV. The corresponding emitted–neutron distributions were essentially isotropic, and the angle–integrated cross sections, given in Table III–2, were obtained assuming isotropy.

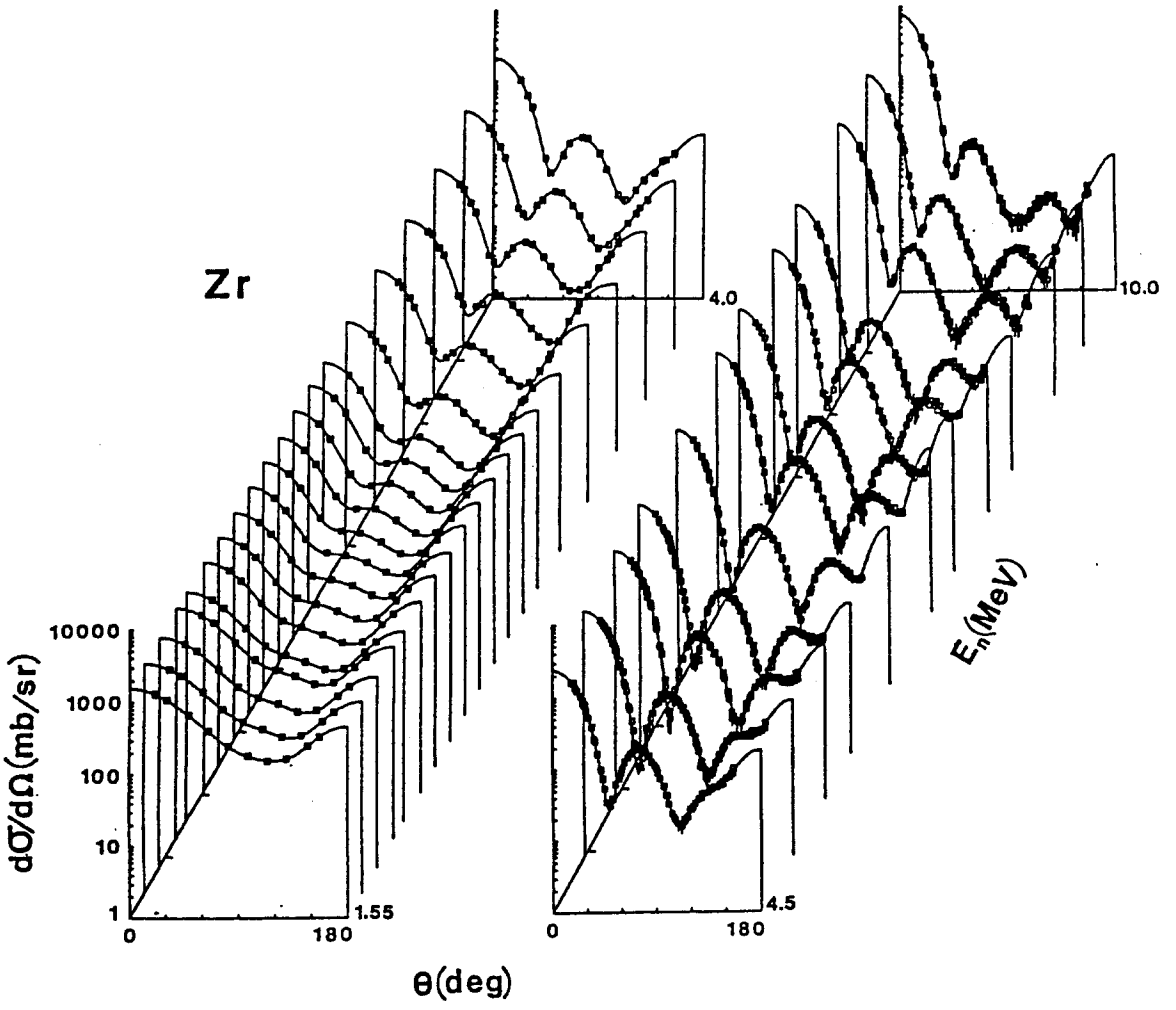

Fig. III–1. Differential elastic–scattering cross sections of elemental zirconium. The present measured values are indicated by data symbols. The curves denote the results of least–square fitting Legendre polynomial expansions to the measured values. The data are given in the laboratory coordinate system.

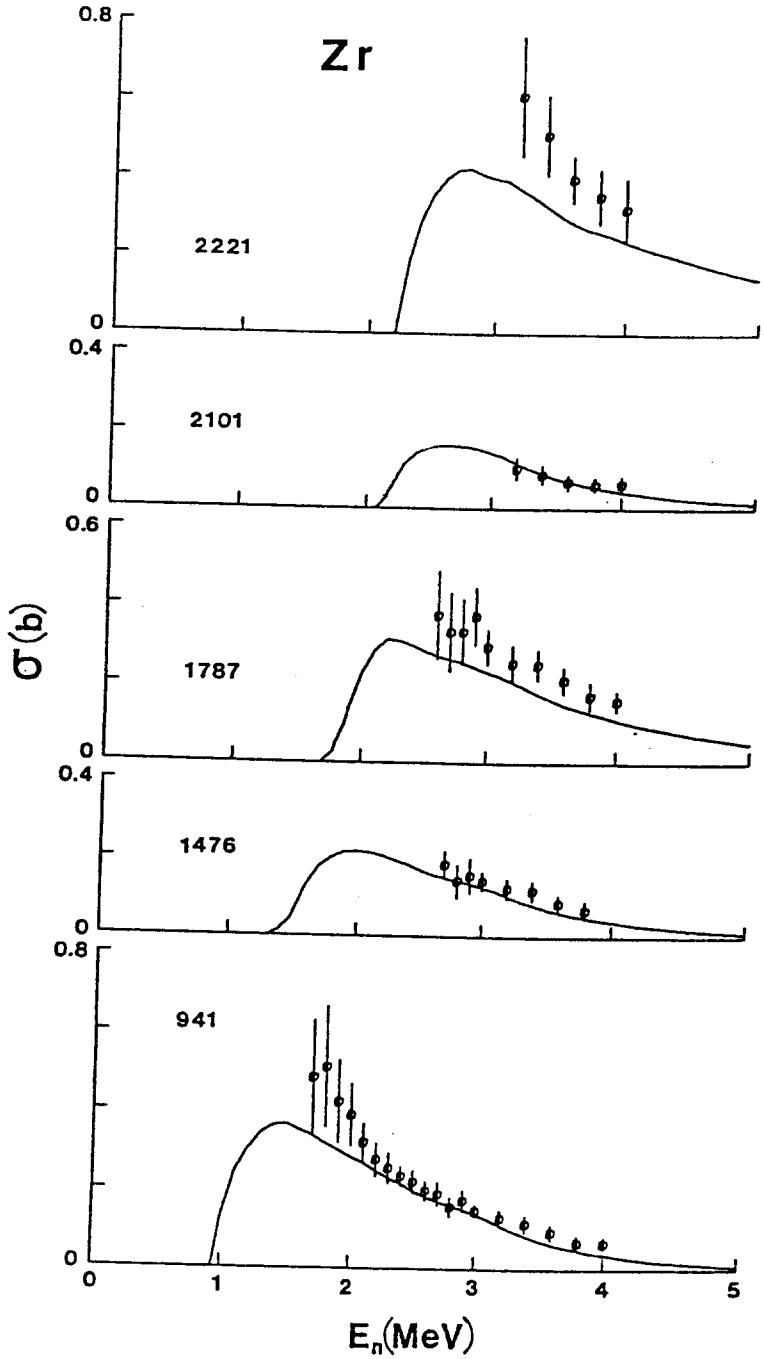

Fig. III–2. Cross sections for the excitation of "elemental" groups in zirconium as defined by Table III–1. Symbols indicate the present experimental results, and curves the calculated values as discussed in Section IV of the text. Observed excitation energies are given in keV.

Table III–1. Discrete inelastic–neutron excitation energies of elemental zirconium (in keV) at incident energies of less than 4 MeV.

		Excitation Energies			
No.	Exp.	^{90}Zr[a]	^{91}Zr[a]	^{92}Zr[a]	^{94}Zr[a]
1	941±25	—	—	934(2+)	919(2+)
2	1476±37	—	1205(1/2+)	1383(0+)	1300(0+)
			1466(5/2+)	1495(4+)	1470(4+)
3	1787±23	1761(0+)	1882(7/2+)	1847(2+)	1671(2+)
4	2101±26	—	2042(3/2+)	2067(2+)	2057(3–)
			2131(9/2+)		
5	2221±17	2187(2+)	many	2150(?)	2151(2+)
6	2363±14	2319(5–)	------- many -------		
7	2791±15	2739(4–)	------- many -------		
		2750(3–)			
8	3101±25	3077(4+)	------- many -------		
9	3331±?	3309(2+)	------- many -------		

[a] Nuclear data sheets as given in Refs. 26 – 29.

Table III-2. Comparisons of measured and calculated compound-nucleus inelastic-scattering cross sections, as discussed in the text.

$E_x \approx 0.941$ MeV

E_{in} (MeV)	14.5 m Flight Path		CN cal.
	$d\sigma/d\Omega$ (mb/sr)	σ (mb)	σ(mb)
6.0	2.6	32.7	2.2
7.0	2.9	36.4	0.6
8.0	2.5	31.4	0.2

$E_x \approx (1.85 - 2.2)$ MeV

E_{in} (MeV)	Flight path			CN cal.
	5 m	14.5 m		
	σ(mb)	$d\sigma/d\Omega$ (mb/sr)	σ (mb)	σ (mb)
4.5	321			307
5.0	235			233
5.5	163			178
6.0	125	11.9	150	137
6.5	107			103
7.0	83	4.6	58	82
8.0		4.4	55	49

$E_x \approx (2.6 - 2.9)$ MeV

E_{in} (MeV)	Flight Path			CN cal.
	5 m	14.5 m		
	σ(mb)	$d\sigma/d\Omega$(mb/sr)	σ(mb)	σ (mb)
5.5	147			162
6.0	133	12.7	160	139
6.5	103			107
7.0	95	5.8	73	85
8.0		3.4	43	53
8.4	54			42

The 14.5 m measurements were limited to one scattering angle, 80°, but gave superior energy resolution. Representative time spectra are shown in Fig. III–3. A general neutron continuum is observed, due to the profusion of levels given in Table III–1. Superimposed upon this are some scattered–neutron groups, the first being the 941 keV "level" of Table III–1. Assuming isotropy of neutron emission, the cross sections of Table III–2 were obtained. As will be discussed in Section IV, these cross sections grossly exceed those predicted by the compound–nucleus process, so that a strong direct–excitation component must be contributing. Thus, the validity of isotropy assumed in deducing the angle–integrated cross section is weak. Two other groups, reasonably in evidence in the long flight–path results, correspond to the two 5 m groups cited above. In these cases, the assumption of isotropic neutron emission is reasonable in deducing angle–integrated cross sections. With this assumption, the results of Table III–2 were obtained. There is fair consistency between the results obtained with the two flight paths, and with the predictions of the compound–nucleus model, as discussed in Section IV. The uncertainties associated with the measured 14.5 m flight–path values in Table III–2 are estimated to be ≈ 10%, with a larger value for the 0.941 MeV group due to its very small cross sections and probable anisotropy.

IV. PHENOMENOLOGICAL OPTICAL–STATISTICAL MODEL

This portion of the data interpretation is based upon the conventional spherical optical–statistical model (SOM).[1] In the present application, the interpretation is complicated by the multi–isotopic nature of the elemental samples used in the measurements. More than half of the element consists of ^{90}Zr (51.45%), and the remaining isotopes are ^{91}Zr (11.27%), ^{92}Zr (17.17%), ^{94}Zr (17.33%), and ^{96}Zr (2.78%).[30] In view of the very small elemental abundance of ^{96}Zr, it was ignored in the present analysis. The remaining four isotopes have quite different excited states, particularly ^{90}Zr, and thus each will have a different compound–elastic–scattering contribution. These differences, together with simple size and asymmetry effects, should be considered in the interpretation if quantitative results are to be obtained. In the present work, a special version of the spherical optical–model code ABAREX was used.[31] This formulation of the code has the capability to least–squares fit the experimental observables, explicitly treating the individual direct and compound–nucleus contributions from up to ten isotopes, and combining them to obtain the elemental result directly comparable with experiment. The excitation of the discrete levels (as well as the statistical level properties) of each of the contributing isotopes were explicitly treated in the fitting. Compound–nucleus processes were calculated using the Hauser–Feshbach theory[32], as corrected for resonance width-fluctuation and correlation effects by Moldauer.[33]

The primary data base for the derivation of the SOM parameters consisted of the present elastic–scattering results extending from ≈ 1.5 to 10 MeV, and shown in Fig. III–1. Elastic scattering at energies of less than 1.5 MeV was not considered, since fluctuations in the cross sections, primarily due to the prominent and closed–shell ^{90}Zr isotope, make the results suspect in the sense that they are not consistent with the energy–average concept of the SOM. To guard against such fluctuations above 1.5 MeV, the data base was averaged over ≈ 200 keV incident–energy intervals up to 4 MeV. Above 10 MeV, only one set of good–quality differential elastic–scattering cross sections was found in the literature, the

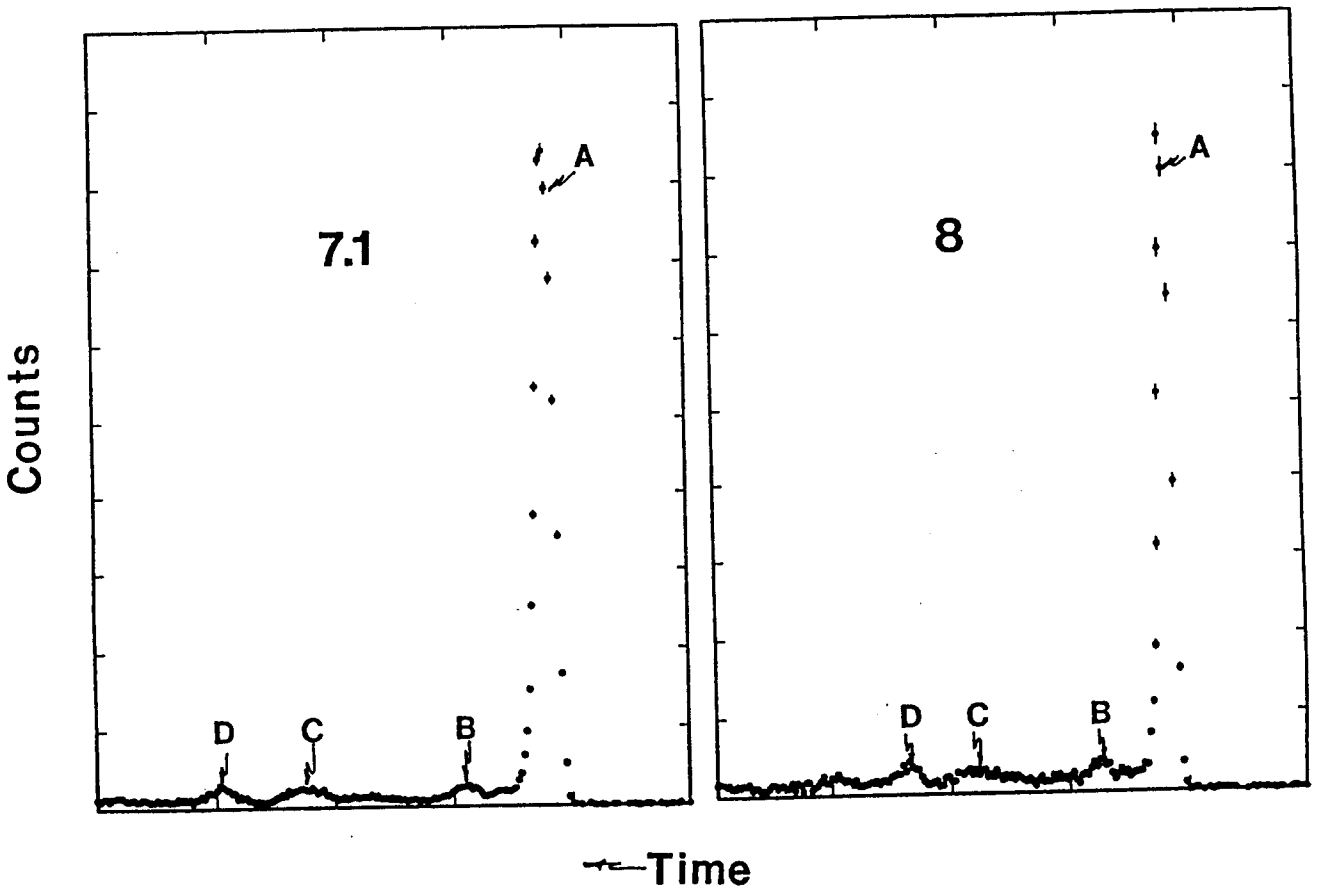

Fig. III–3. Observed time spectra obtained by scattering 7.1 (left) and 8.0 MeV (right) neutrons from elemental zirconium. The scattering angle is 80° and the flight path 14.52 m. The measured values are indicated by symbols, and prominent average excitations by A = elastic scattering, B = inelastic excitation of the 941 keV "group", C = neutrons from excitations in the range of $\approx 1.85 - 2.2$ MeV, and D = contributions from excitations of $\approx 2.6 - 2.9$ MeV.

24–MeV distributions of Refs. 5 and 6. Although the latter results are isotopic, an elemental distribution was constructed. It was added to the primary data base to provide a higher–energy elastic–scattering distribution for the fitting. This data base was explicitly least–square fitted to determine the SOM parameters, as described below. The fitting involved minimizing the expression

$$\chi^2 = \frac{1}{N}\sum_{i=1}^{N}\left[\frac{\sigma_i(\text{exp}) - \sigma_i(\text{cal})}{\delta\sigma_i(\text{exp})}\right]^2. \qquad \text{(IV–1)}$$

The results of the analysis were compared with the elemental neutron total cross section, as summarized in Ref. 34, and with the isotopic s– and p–wave strength functions, although these observables were not a part of the fitting procedure.

All the discrete levels[26–29] below 4 MeV in ^{90}Zr, and below 3 MeV in ^{91}Zr, ^{92}Zr, and ^{94}Zr, were taken into account in these calculations. These 71 states are listed in Table IV–1. Although most of them have known J^π values, a few cases were ambiguous. However, these were all at fairly high excitation energy, where many exit channels are open, so that the calculated results are not very sensitive to the assumed J^π estimates. The effect of compound–nucleus processes involving excitations above the discrete levels was calculated using the statistical level representation of Gilbert and Cameron.[35] Those authors explicitly give temperatures (T), E_0 values, and spin cutoff factors (σ) for ^{92}Zr and ^{94}Zr. They also provide formulae from which values were calculated for ^{90}Zr and ^{91}Zr. These statistical parameters are summarized in Table IV–2. They reasonably extrapolate to the known discrete level structure, and modest variations in them do not significantly change the results of the fitting.

The SOM was assumed to have Woods–Saxon and derivative Woods–Saxon forms for the real and imaginary potentials, respectively, and a Thomas spin–orbit term.[1] Although the neutron polarization is sensitive to the spin–orbit potential, the Zr elastic scattering is not. Since comprehensive polarization data are not available for the Zr isotopes, the choice of this interaction is somewhat arbitrary. Throughout most of the present analysis it was assumed that

$$\begin{aligned} V_{so} &= 5.5 \text{ MeV} \\ r_{so} &= 1.005 \text{ fm} \\ a_{so} &= 0.65 \text{ fm}. \end{aligned} \qquad \text{(IV–2)}$$

These parameters are similar to those given for global SOM's, as deduced when polarization data were available.[7] (Throughout this paper, radii are expressed in the form $R_i = r_i \cdot A^{1/3}$).

Consider the central SOM potentials. If, for example, the global 10–MeV parameters of Walter and Guss[7] were used, the effect of the isovector interaction, the

Table IV-1. Discrete level structure employed in the calculations. E_x is the excitation in MeV and J^π are the spin and parity values assumed in the calculations.

^{90}Zr[a]		^{91}Zr[b]		^{92}Zr[c]		^{94}Zr[d]	
E_x	J^π	E_x	J^π	E_x	J^π	E_x	J^π
0.0	0^+	0.0	$5/2^+$	0.0	0^+	0.0	0^+
1.761	0^+	1.205	$1/2^+$	0.934	2^+	0.919	2^+
2.187	2^+	1.466	$5/2^+$	1.383	0^+	1.300	0^+
2.319	5^-	1.882	$7/2^+$	1.495	4^+	1.470	4^+
2.739	4^-	2.042	$3/2^+$	1.847	2^+	1.671	2^+
2.750	3^-	2.131	$9/2^+$	2.067	2^+	2.058	3^-
3.077	4^+	2.170	$11/2^-$	2.340	3^-	2.151	2^+
3.309	2^+	2.190	$5/2^-$	2.398	4^+	2.330	4^+
3.448	6^+	2.201	$7/2^+$	2.486	5^-	2.366	2^+
3.589	8^+	2.260	$13/2^-$	2.744	4^-	2.508	3^+
3.843	2^+	2.288	$15/2^-$	2.820	2^+	2.605	5^-
3.976	5^-	2.321	$11/2^-$	2.864	4^+	2.699	1^+
--		2.357	$1/2^-$	2.904	0^+	2.826	3^-
--		2.367	$7/2^-$	2.958	6^+	2.846	2^+
--		2.395	$9/2^-$	--		2.861	5^-
--		2.535	$3/2^+$	--		2.908	2^+
--		2.558	$1/2^+$	--		--	
--		2.578	$5/2^-$	--		--	
--		2.640	$3/2^-$	--		--	
--		2.694	$7/2^-$	--		--	
--		2.765	$13/2^-$	--		--	
--		2.775	$5/2^-$	--		--	
--		2.811	$5/2^-$	--		--	
--		2.826	$3/2^+$	--		--	
--		2.857	$13/2^+$	--		--	

Table IV-1 (Continued)

^{90}Zr[a]		^{91}Zr[b]		^{92}Zr[c]		^{94}Zr[d]	
E_x	J^π	E_x	J^π	E_x	J^π	E_x	J^π
--		2.874	$3/2^+$	--		--	
--		2.902	$7/2^+$	--		--	
--		2.914	$9/2^+$	--		--	
--		2.928	$3/2^+$	--		--	

[a] D. C. Kocher, Nuclear Data Sheets 16 55 (1975).
[b] H. W. Muller, Nuclear Data Sheets 31 181 (1980); 60 835 (1990).
[c] P. Luksch, Nuclear Data Sheets 30 573 (1980).
[d] H. W. Muller, Nuclear Data Sheets 44 277 (1985).

Table IV-2. Statistical parameters used in the calculations.[35]

Isotope	Temperature (MeV)	E_0 (MeV)	spin cutoff
^{90}Zr	0.854	1.00	3.37
^{91}Zr	0.831	0.04	3.42
^{92}Zr	0.740	1.01	3.35
^{94}Zr	0.760	0.84	3.65

(N–Z)/A term[4] would be to decrease the real and imaginary strengths by about 1.2% and 7.4%, respectively, in going from ^{90}Zr to ^{94}Zr. Such changes were examined and found to have little impact, and hence they were neglected in the subsequent analysis. In addition, even though the data base extended to 24 MeV, no evidence was found for any significant volume absorption. When the latter potential was included in the fitting, its strength turned out to be very nearly zero, in agreement with the findings of Wang and Rapaport.[6]

The SOM parameter search started by varying the real and imaginary strengths, radii, and diffusenesses. The initial emphasis was given to the determination of the real potential, as it is expected to be less sensitive to detailed nuclear–structure effects than the imaginary interaction. The resulting real radius, r_v, decreased with energy in an approximately linear manner, as described by

$$r_v = (1.310 - 0.0063 \cdot E) \text{ fm}, \tag{IV–3}$$

where, throughout this paper, E is the incident–neutron laboratory energy in MeV. (Herein, potential parameters are cited to high precision, so that the calculational results can be accurately reproduced.) The data base was refitted, fixing r_v to this value and varying the remaining five parameters. The resulting real diffuseness was essentially constant with energy, with the average value of

$$a_v = 0.667 \text{ fm}. \tag{IV–4}$$

The fitting then proceeded to the remaining four–parameters. This resulted in the imaginary radius of

$$r_w = (1.39 - 0.0063 \cdot E) \text{ fm}. \tag{IV–5}$$

Fixing r_w, three–parameter searches then gave

$$a_w = (0.310 + 0.018 \cdot E) \text{ fm}. \tag{IV–6}$$

Finally, the real and imaginary strengths were determined from two–parameter fitting, using the above fixed geometric parameters. The strengths were expressed in the form of volume–integrals–per–nucleon, J_i,

$$J_i = \frac{4\pi}{A} \int V_i(r)\, r^2\, dr, \tag{IV–7}$$

where "i" is "v" or "w" for real and imaginary strengths, respectively. The values of J_v and J_w, shown in Fig. IV–1, were deduced from the strengths and geometries of the optical-model potentials, assuming that A = 91.3 (i. e., the weighted average for the elemental sample). From Fig. IV–1, it is clear that the J values resulting from the fitting varied in an approximately linear manner with energy. The uncertainties in these J_i values are related in a complex manner to the model interpretation and the underlying data. For

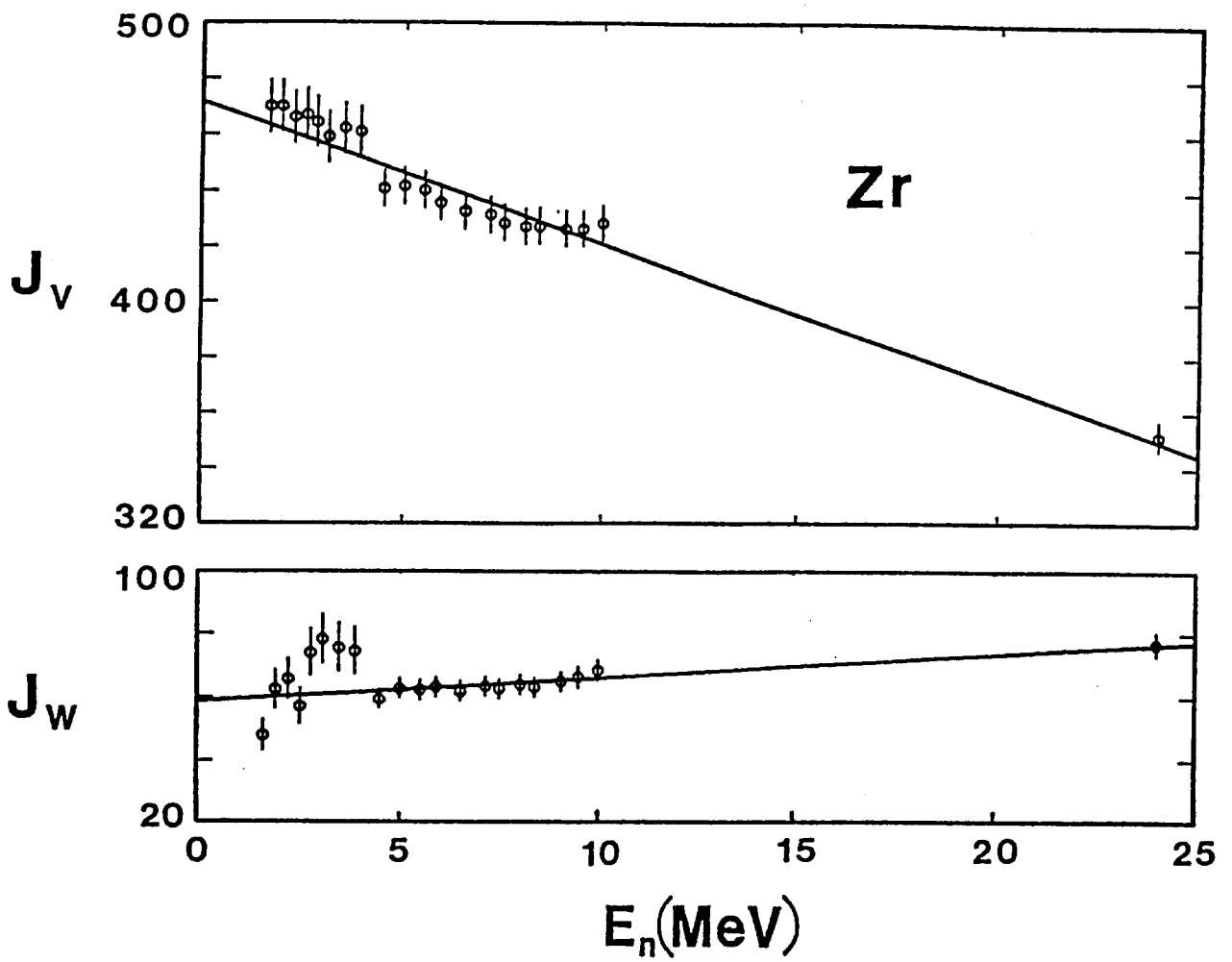

Fig. IV–1. Real (J_v) and imaginary (J_w) volume integrals per nucleon as a function of incident energy for the SOM. Experimentally–deduced values are indicated by symbols and the results of the linear fits of Eqs. IV–8 and –9 by solid lines. The J_i units are MeV–fm^3.

J_v, they are estimated to be ≈ 1.5% above 4 MeV and ≈ 2% at lower energies, as illustrated in Fig. IV–1. A least–squares fit to these values gives

$$J_v = (471.17 - 5.09 \cdot E) \ \text{MeV–fm}^3. \qquad \text{(IV–8)}$$

There is more scatter in the J_w values, particularly at energies below ≈ 4 MeV where the results are sensitive to the detailed nature of the statistical parameters of Table IV–2, and to residual cross–section fluctuations. At these lower energies the uncertainties in J_w are estimated to be ≈ 10%, while above 4 MeV the error is ≈ 5%. Again, a least–squares fit, taking into account the estimated uncertainties, gives

$$J_w = (58.36 + 0.74 \cdot E) \ \text{MeV–fm}^3. \qquad \text{(IV–9)}$$

On the other hand, if one limits the fit to energies above 4 MeV,

$$J_w = (57.17 + 0.83.E) \ \text{MeV–fm}^3. \qquad \text{(IV–10)}$$

The two results are consistent within the uncertainties estimated for individual J_w values.

The results calculated with the model described above are compared in Fig. IV–2 with the experimental data from which it was developed. The agreement between measured and calculated results is generally very good, and the differences are probably not significantly larger than the experimental uncertainties. The same model gives a good description of the elemental zirconium energy–averaged neutron total cross section from a few keV to at least 20 MeV as illustrated in Fig. IV–3. The measured and calculated values agree to within several percent over the entire energy range.

To apply this model to the data observed for the various zirconium isotopes, one must make some assumption about the $(N - Z)/A$ dependence of the deduced potentials. For this purpose, we assume that J_v can be expressed in the form

$$J_v = J_o\left[1 + \alpha_v \cdot ((N - Z)/A)\right] + \beta_v \cdot E, \qquad \text{(IV–11)}$$

with J_o and α_v independent of energy, E, and β_v independent of $(N - Z)/A$. The global models of Walter and Guss[7], and of Rapaport[8], give $\alpha_v = -0.31$ and -0.42, respectively. The fitting of the separated–isotope data at 8, 10 and 24 MeV[6] leads to $\alpha_v = -0.35$ (intermediate between the two global values), and we shall use this value. In order that J_v have the value given by Eq. IV–8 (when Z = 40, N = 51.3 and A = 91.3), it follows that

$$J_v = \left[492.50(1 - 0.35 \cdot ((N - Z)/A)) - 5.09 \cdot E\right] \ \text{MeV–fm}^3. \qquad \text{(IV–12)}$$

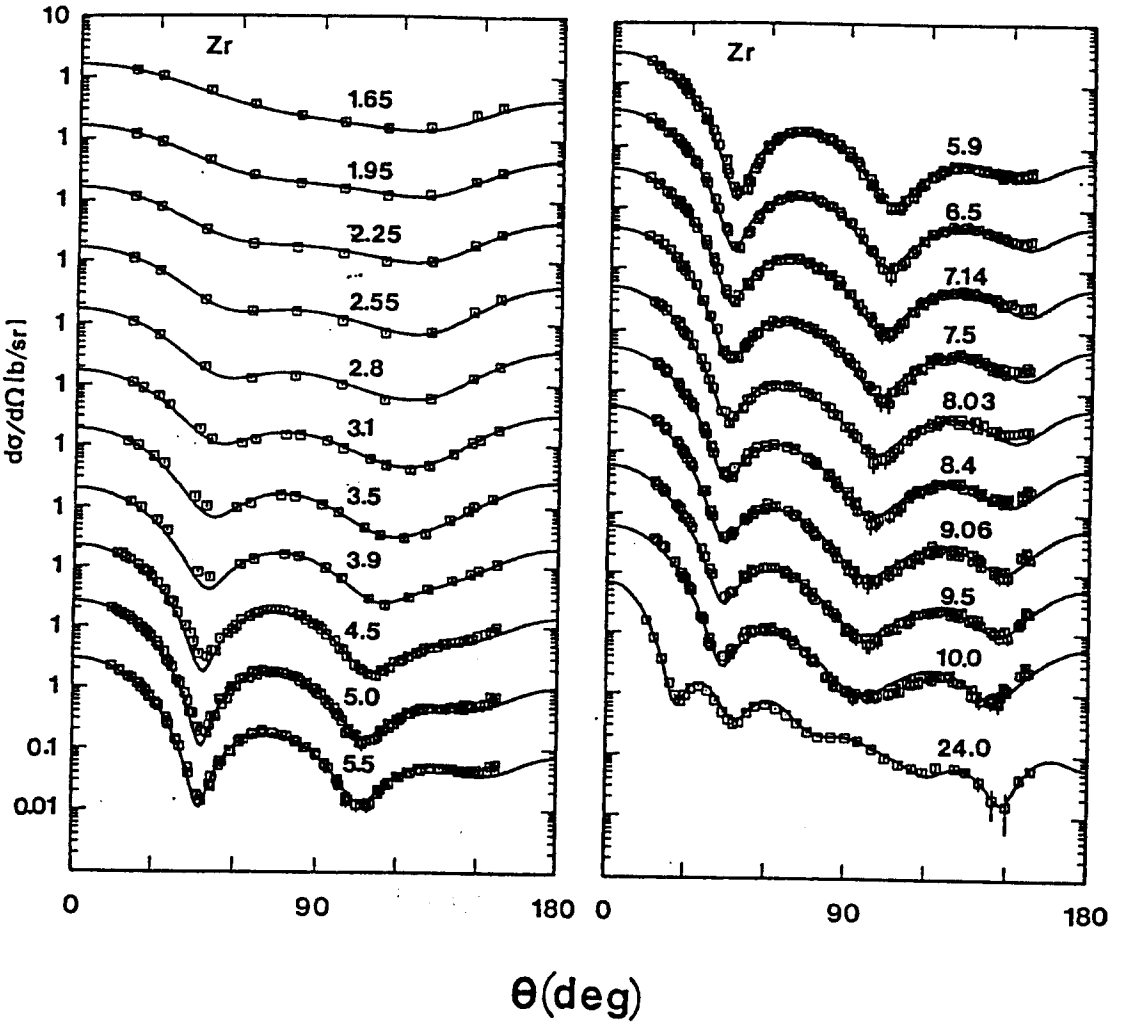

Fig. IV–2. Comparison of measured and calculated elastic–scattering cross sections of elemental zirconium. The results obtained with the SOM are indicated by curves. The measured data are indicated by "□" symbols, where all results for E ≤ 10 MeV are from the present work, and the 24 MeV distribution from ref. 6. Incident energies are numerically given in MeV. The data are in the laboratory coordinate system.

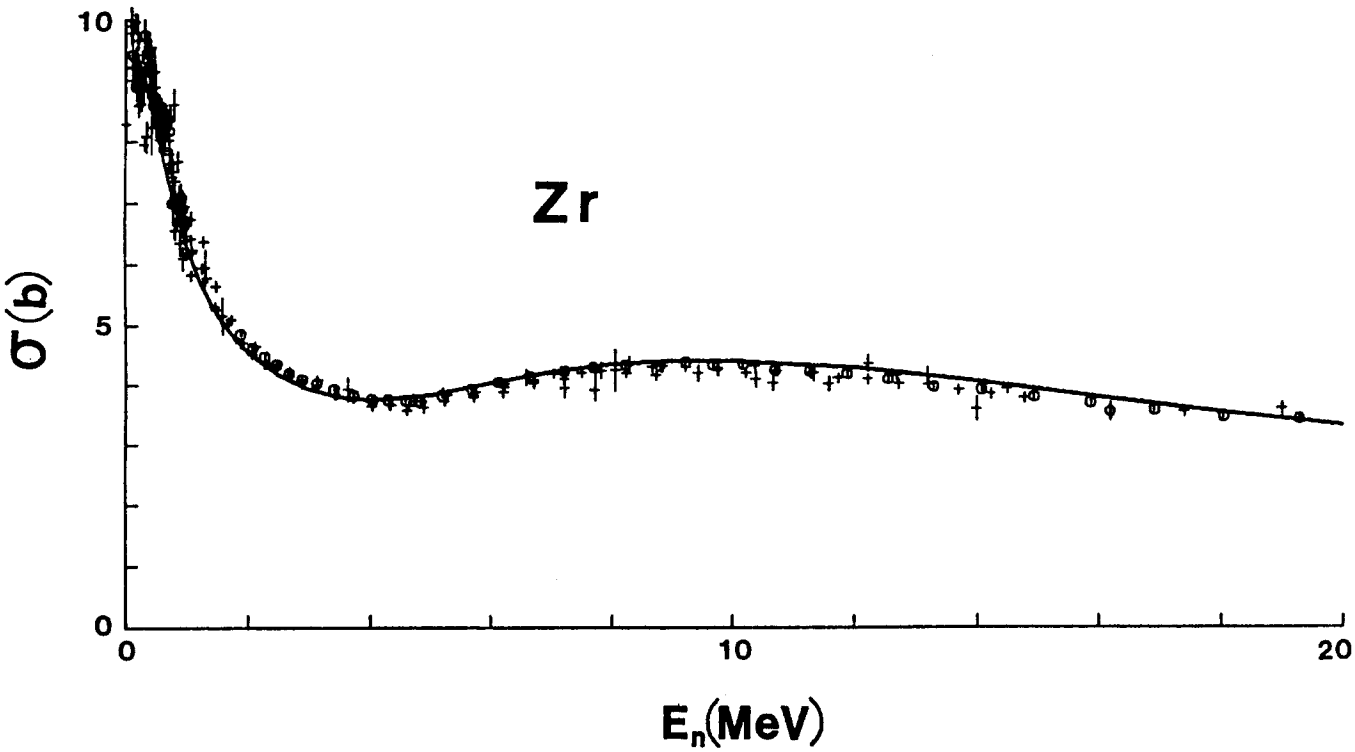

Fig. IV–3. Comparison of measured (symbols) and SOM–calculated (curve) neutron total cross sections of elemental zirconium. The various experimental values are taken from the literature as described in ref. 34.

A similar expression can be written for J_w. According to the global models,[7,8] α_w is negative and has an absolute magnitude greater than unity. On the other hand, the zirconium isotopic data[6] clearly indicate that J_w increases with increasing $(N - Z)/A$ — in other words, the sign is opposite to that given by the global models. This is understandable, since ^{90}Zr has fifty neutrons, and it is well known that J_w increases rapidly as one moves away from a closed shell.[10] Physically, W is a measure of the softness (ease of excitation) of the core, and it is widely recognized that closed–shell nuclei have stiffer cores (i.e., fewer low–lying states with smaller excitation probabilities). The Zr isotopic data of Wang and Rapaport[6] indicates that α_w could be as large as $5 - 10$. However, in view of the uncertainties in the data, and the derivation of the model from the data, we feel that a more realistic estimate of α_w is probably about 2. Accepting this, one finds that in order for J_w to have the values given by Eq. IV–9 (for $Z = 40$, $N = 51.3$, and $A = 91.3$),

$$J_w = \left[46.78(1 + 2\cdot((N - Z)/A)) + 0.74\cdot E\right] \text{ MeV–fm}^3. \qquad \text{(IV–12)}$$

The low–energy strength functions deduced from resonance measurements were not a part of the data base used in the fitting. However, the values calculated, using the model and the potential strengths given by Eqs. IV–11 and –12, are in reasonable agreement with those deduced from resonance measurements,[36] as shown in Table IV–3. The predicted s–wave strength function decreases slightly as one goes to the heavier isotopes. Concurrently, the p–wave values increase. Although the experimentally derived data have a great deal of scatter, they do exhibit the same general mass–dependent trends. Since the model has only a smooth dependence on $(N - Z)/A$, it cannot reproduce the fluctuations evident in the experimentally based data, which may reflect detailed differences in nuclear

Table IV–3. Comparison of measured and calculated strength functions (X 10^4) for the isotopes of zirconium.

Isotope	s–wave strength function		p–wave strength function	
	Exp.	Cal.	Exp.*	Cal.
^{90}Zr	0.7±0.2	0.64	4.0±0.6	5.19
^{91}Zr	0.36±0.08	0.63	6.7±1.3	5.45
^{92}Zr	0.50±0.10	0.62	7.0±1.3	5.69
^{94}Zr	0.50±0.15	0.61	9.8±2.0	6.10
^{96}Zr	0.34±0.14	0.59	6.0±1.8	6.40

* From Ref. 36.

structure, small resonance samples, or other experimental uncertainties. The calculated scattering length, R′, decreases from 6.98 fm for ^{90}Zr to 6.88 fm for ^{96}Zr, and is in reasonable agreement with the experimentally deduced value of (7.2 ± 0.2) fm.[36]

In Figs. IV–4 and –5, the predictions of the model, with the potential strengths of Eqs. IV–11 and –12, are compared with experiment. The data for the two isotopes, ^{90}Zr and ^{92}Zr, are fairly extensive,[6,37,38] and agreement between measured and calculated results is remarkably good from 1.5 to 24 MeV, as illustrated in Fig. IV–4. The experimental data[6,39] for ^{91}Zr and ^{94}Zr are fewer, but again the model appears suitable, as shown in Fig. IV–5.

As discussed in Section III, it is difficult to relate observed elemental inelastic-scattering cross sections to the excitation of specific levels in individual isotopes. However, there is some isotopic inelastic–scattering information reported in the literature (summarized in Ref. 34) which is primarily confined to inelastic–scattering from ^{90}Zr and ^{92}Zr. Some of these experimental results are compared with the predictions of the model in Figs. IV–6 and –7. Given the experimental uncertainties, the agreement is acceptable. The calculated results are also compared with the present elemental measurements in Fig. III–2. Agreement between the first few measured and calculated excitations is reasonably good at low incident energies where the processes are primarily due to compound–nucleus reactions. However, the complex elemental level structure makes comparisons for the higher–energy excitations less reliable because of limited experimental resolution. At higher incident energies, the inelastic scattering is essentially a continuum distribution, upon which is superimposed some structure due to clumps of levels, as illustrated in Fig. III–3. The measured composite inelastic–scattering cross sections are summarized in Table III–2. The inelastic–scattering cross sections implied by the two prominent scattered-neutron groups (corresponding to observed excitations of ≈ 2.05 and 2.75 MeV) are in good agreement with the predictions of compound–nucleus calculations obtained using the model. However, the cross section at, for example, 8 MeV for the excitation of the "941 keV group" is two orders of magnitude larger than predicted by compound–nucleus calculations. The observed excitation is primarily due to the yrast 2^+ levels in ^{92}Zr and ^{94}Zr, and these are known to have a strong direct–reaction component. For example, at 8 MeV the work of Wang and Rapaport[6] indicates similar 2^+ excitations for ^{92}Zr and ^{94}Zr with a cross–section magnitude of ≈ 60 mb. Thus, the direct–reaction contributions of these two isotopes to the "941 keV group" in elemental zirconium would be about 20 mb, and this is in fairly close agreement with the value given in Table III–2. Similarly, direct–reactions undoubtedly contribute to the higher–energy cross sections listed in Table III–2, but their effects are not as dramatic as those of the "941 keV group" since, in these cases, the compound–nucleus cross section is ≈ 50 mb.

The need for direct–reaction contributions can be further illustrated by Monte-Carlo simulations[40] of the observed velocity spectra. In Fig. IV–8, the expected velocity spectrum, equivalent to the examples of Fig. III–3, is simulated using compound–nucleus inelastic–scattering cross sections calculated with the model. For the two higher–energy groups, the simulated results are qualitatively similar to the experimental distributions given in Fig. III–3, even though the detector energy dependence has not been considered in the simulation, and the Monte–Carlo results are binned into relatively wide, 15°, angular increments. However, the compound–nucleus–based simulation results in a spectrum that

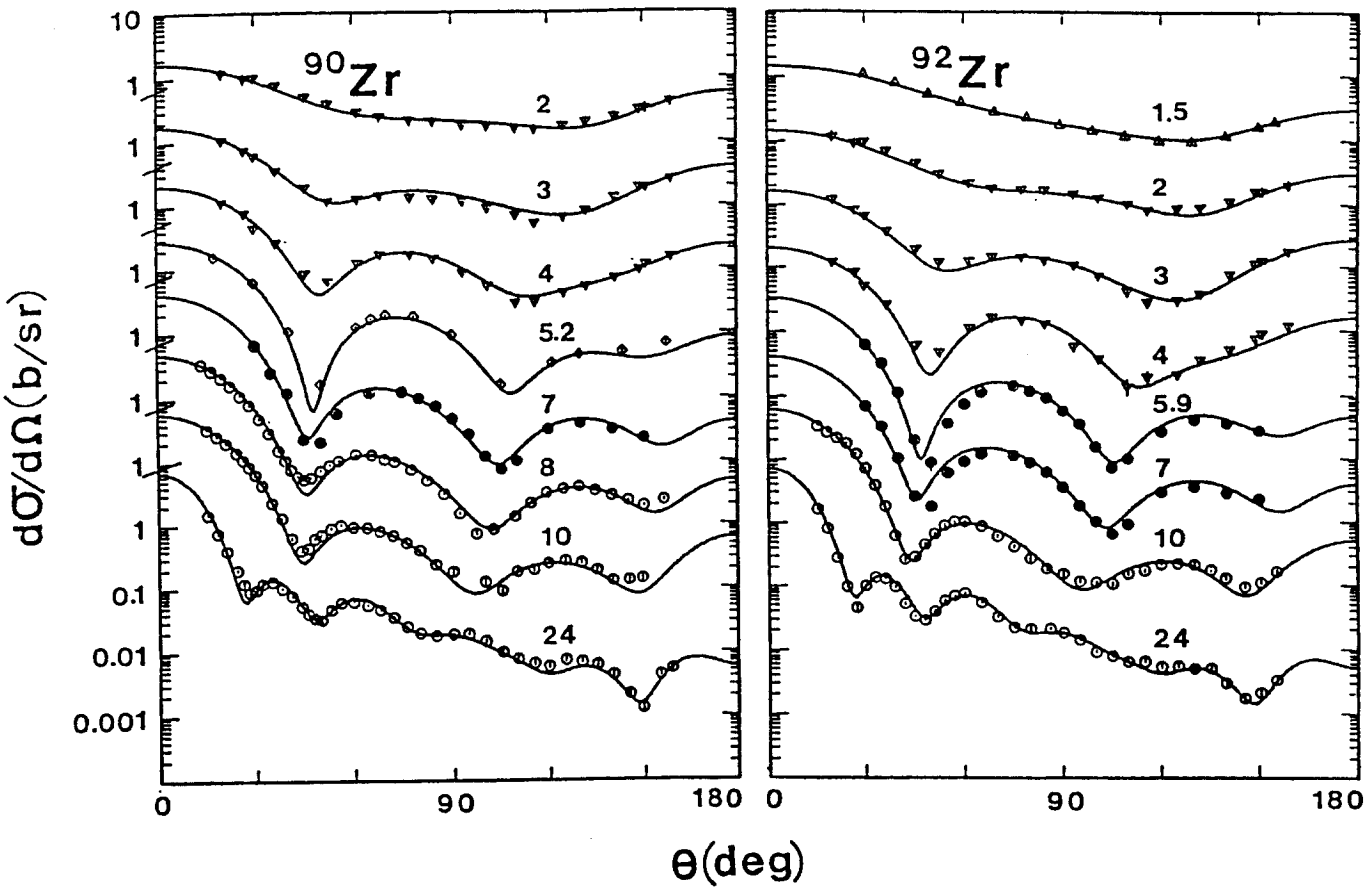

Fig. IV–4. Comparison of measured (symbols) and calculated (curves) differential elastic–scattering cross sections of ^{90}Zr and ^{92}Zr. The measured values were taken from refs. 6, 37 and 38, and the calculations used the SOM potential. Incident energies are numerically given in MeV. The data are given in the laboratory coordinate system.

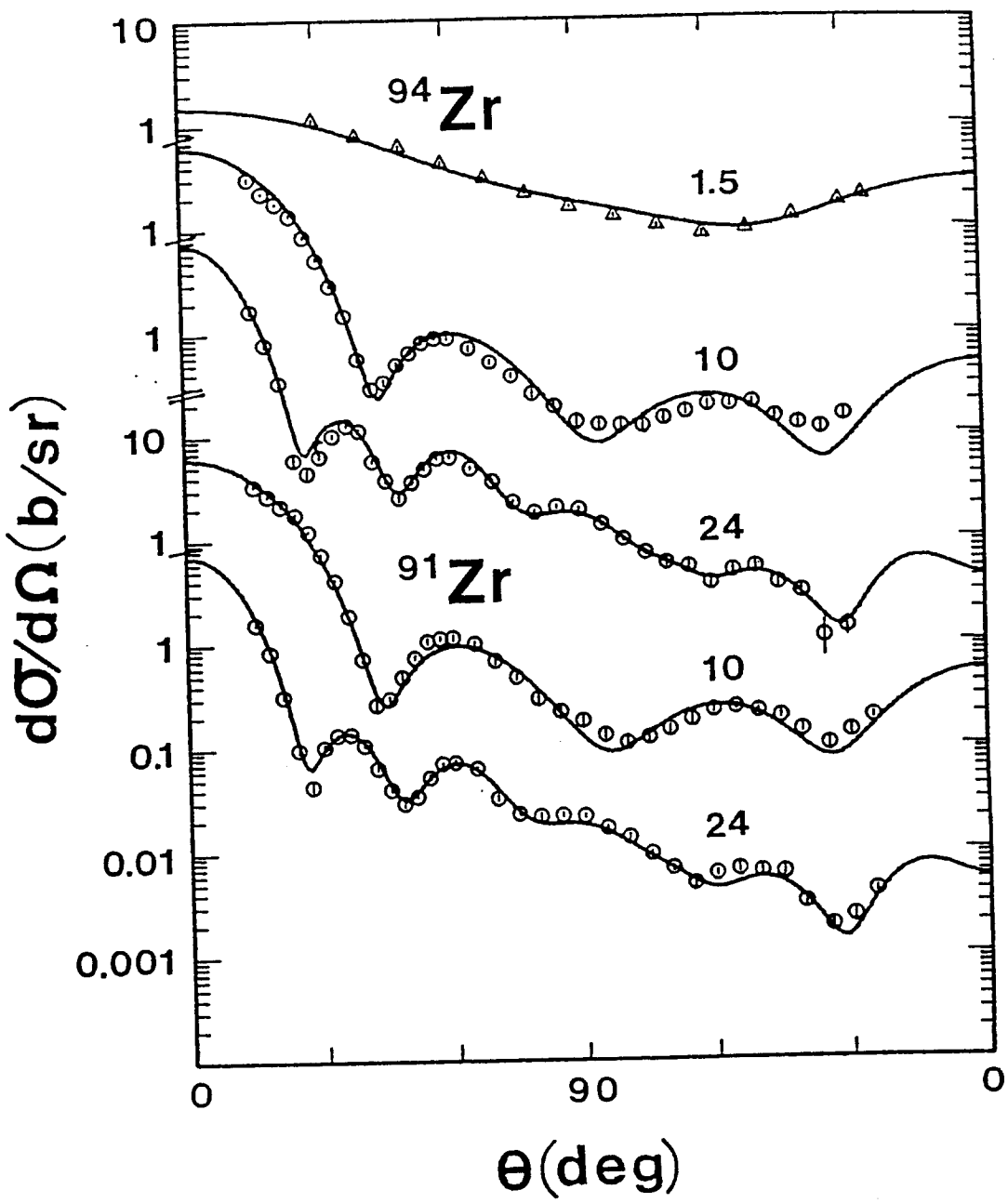

Fig. IV–5. Comparisons of measured (symbols) and calculated (curves) differential elastic–scattering cross sections of ^{91}Zr and ^{94}Zr. The measured values were taken from refs. 6 and 39, and the calculations used the SOM potential of the present work. Incident energies are numerically given in MeV. The data are given in the laboratory coordinate system.

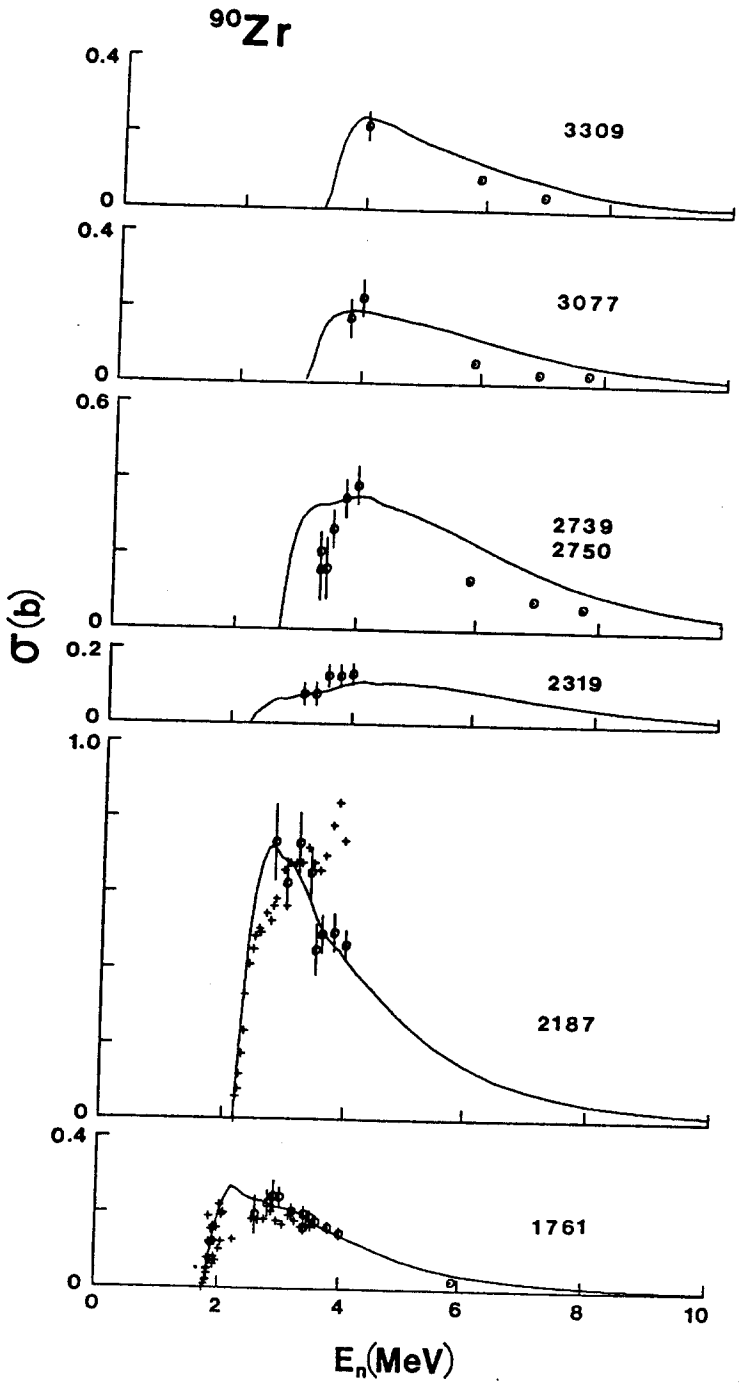

Fig. IV–6. Illustrative comparisons of measured (symbols)[34] and SOM–calculated (curves) cross sections for the excitation of specific levels in ^{90}Zr. Level excitation energies are given in keV.

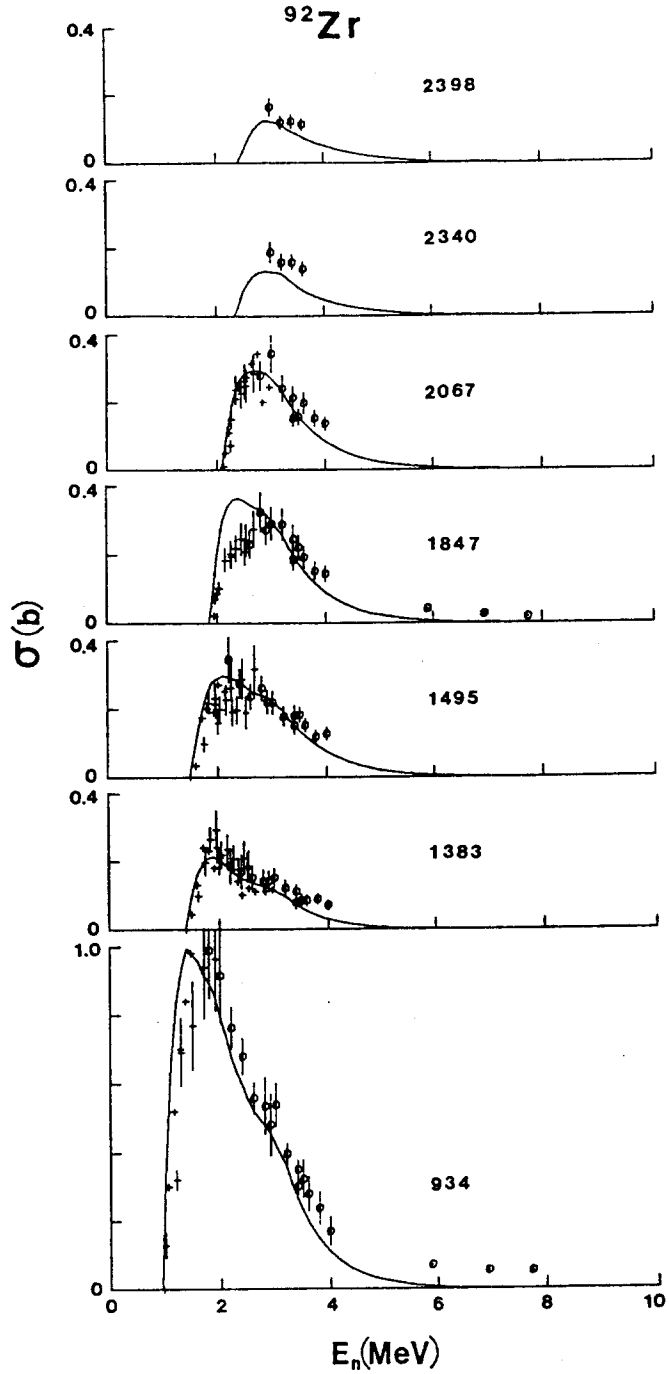

Fig. IV–7. Illustrative comparisons of measured (symbols)[34] and SOM–calculated (curves) cross sections for the excitation of specific levels in ^{92}Zr. The notation is identical to that of Fig. IV–6.

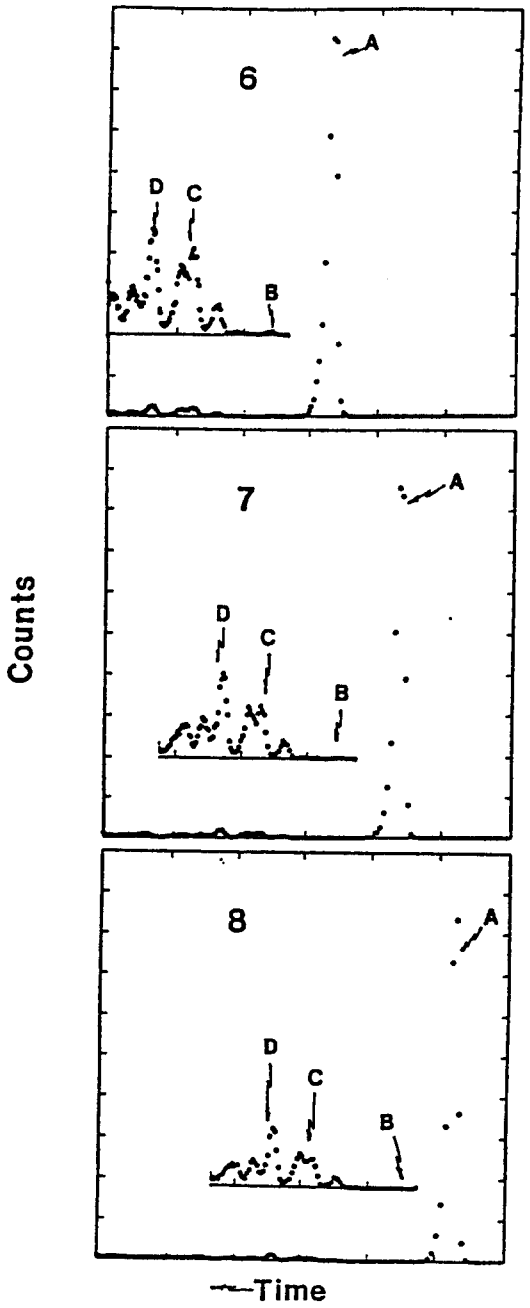

Fig. IV–8. Velocity spectrum resulting from the Monte–Carlo simulation described in the text. Incident energies are numerically noted in MeV. The scattering angle is 80^{O} and flight path 14.5 m. A, B, C and D notations have the same connotation as in the caption of Fig. III–3. The inelastic–neutron groups can be associated with the isotopic level structure given in Tables III–1 and IV–1.

has very little evidence for inelastic excitation of the "0.941 MeV group", in disagreement with experiment. Furthermore, a comparison of Figs. III–3 and IV–8 suggests a very small continuum of inelastically–scattered neutrons, throughout the energetically accessible region, that is not consistent with a purely discrete compound–nucleus representation. This suggests that small pre–compound processes may contribute to a number of the inelastic–scattering cross sections.

In fitting the elemental zirconium data, the size dependence ($R_i = r_i A^{1/3}$) was taken into account, but the potential strengths were assumed to be the same for all isotopes of the sample, i.e., the $(N - Z)/A$ dependence of the strengths was assumed to be unimportant. We now return to quantitatively address this assumption. The darker curve in Fig. IV–9 shows the predicted 10–MeV elastic–scattering cross sections for the various isotopic constituents of elemental zirconium, when size variation is taken into account, but the potential strengths (given by Eqs. IV–8 and –9 with A = 91.3) are assumed to be the same for each isotope. The lighter curves show the effects of varying size, and also including the isovector component of the potentials — that is taking different strengths for each isotope deduced from Eqs. IV–11 and –12. For A = 91 and 92, the two results are indistinguishable. For A = 90, they differ only at very large angles where no data exist. Thus, for nearly 80% of the sample there is no experimentally observable effect of the $(N - Z)/A$ dependence of the potential. There are only slight differences between the two curves near the minima of the ^{94}Zr distribution, but these are smaller than the relevant experimental uncertainties. It is only for ^{96}Zr that the differences are significant, and this isotope is less than 3% abundant. Thus, the assumption in the elemental fitting that the isovector effects could be ignored is valid.

V. THE DISPERSIVE OPTICAL MODEL

In the preceding section, a conventional SOM was used to interpret the neutron elastic–scattering data of elemental zirconium. In this analysis it was found that only the diffuseness of the real potential was energy independent, whereas all of the other geometrical properties of the SOM depended on E. Since the foregoing analysis did not explicitly take into account the fundamental dispersion relationship[2] which links real and imaginary potentials, it is of interest to see what happens when this feature is incorporated.

The dispersion relationship connects the real and imaginary OM potentials, or radial moments of these interactions, by the expression

$$V(r,E) = V_{HF}(r,E) + \frac{P}{\pi}\int_{-\infty}^{+\infty}\frac{W(r,E')dE'}{(E-E')} , \qquad (V-1)$$

where V(r,E) and W(r,E) are the total real and imaginary potentials, respectively, $V_{HF}(r,E)$ is the Hartree–Fock component, and P denotes the principal value integral. In the SOM of the preceding section, a derivative Woods–Saxon form was used for the imaginary potential. This implies that the real interaction should have a surface component. In order to estimate the magnitude of this surface component, consider Eq. V–1, as expressed in terms of volume–integral–per–nucleon,

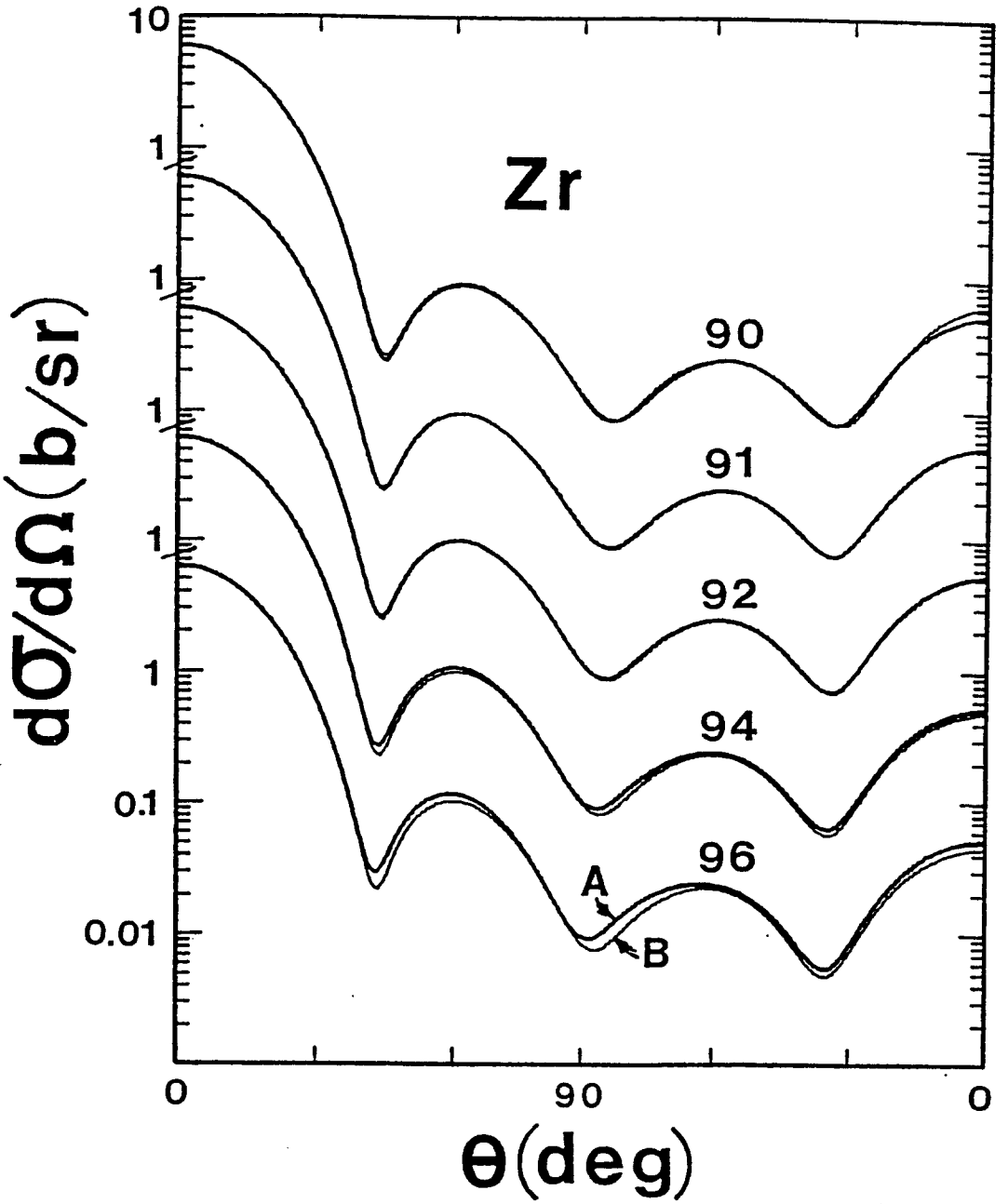

Fig. IV–9. The effect of the isovector potential on the 10 MeV elastic–scattering from the isotopes of zirconium. The heavy curves (A) were calculated using the same potential strengths (Eqs. IV–8 and –9, $A = 91.3$) and taking into account the $R_i = r_i \cdot A^{1/3}$ size effect for each isotope. The light curves (B) included the $(N - Z)/A$ dependence of the potential strengths as given by Eqs. IV–11 and –12.

$$J_v(E) = J_{eff}(E) + \frac{P}{\pi}\int_{-\infty}^{+\infty} \frac{J_s(E')\,dE'}{(E-E')} . \qquad (V-2)$$

In this expression, $J_s(E)$ is the surface–peaked component of the imaginary potential, given by Eq. IV–9, and $J_{eff}(E)$ is the sum of the contribution due to $V_{HF}(E)$ and any additional volume absorption which was not considered in the preceding discussion. (We shall return to this point later.) In order to evaluate the effect of the surface interaction, dJ_s, on the real potential we define,

$$dJ_s \equiv \frac{P}{\pi}\int_{-\infty}^{+\infty} \frac{J_s(E')dE'}{(E-E')} , \qquad (V-3)$$

where $J_s(E)$ must be known for all values of E. In order to estimate this quantity, $J_s(E)$ is assumed to be:

i) Symmetric about the Fermi energy, E_F, where

$$E_F = 1/2\,(\epsilon_d + \epsilon_g) = -9.6 \text{ MeV} , \qquad (V-4)$$

and ϵ_d and ϵ_g are the binding energies of the $d_{5/2}$ and $g_{9/2}^{-1}$ neutron states to the ^{90}Zr core.

ii) For $2\cdot E_F \le E \le 0$, $J_s = J_o\cdot(E-E_F)^2/E_F^2$, where $J_o = 58.36$ MeV fm^3 is the value of J_s at E = 0 (see Eq. IV–9).

iii) For $0 \le E \le 25$ MeV, J_s has the values given by Eq. IV–9.

iv) For $E \ge 25$ MeV, J_s decreases linearly with energy to 0 at 60 MeV, and remains 0 at higher energies.

With these assumptions, $dJ_s(E)$ was evaluated. The results are shown in Fig. V–1 (curve labeled "dJ_s"). In the upper half of this figure, the ratio

$$R(E) = dJ_s(E)/J_s(E) \qquad (V-5)$$

is shown, and this is the factor by which the imaginary potential should be multiplied to give the surface–peaked component of the real OM potential.

With the spin–orbit parameters held fixed to the values given by Eq. IV–2, a fit to the Zr elastic–scattering data base, including the surface–peaked real component, was carried out in the same way as discussed in the previous section for the SOM. Actually, since $dJ_s(E)$ and R(E) depend on the deduced imaginary potential, one should repeat the

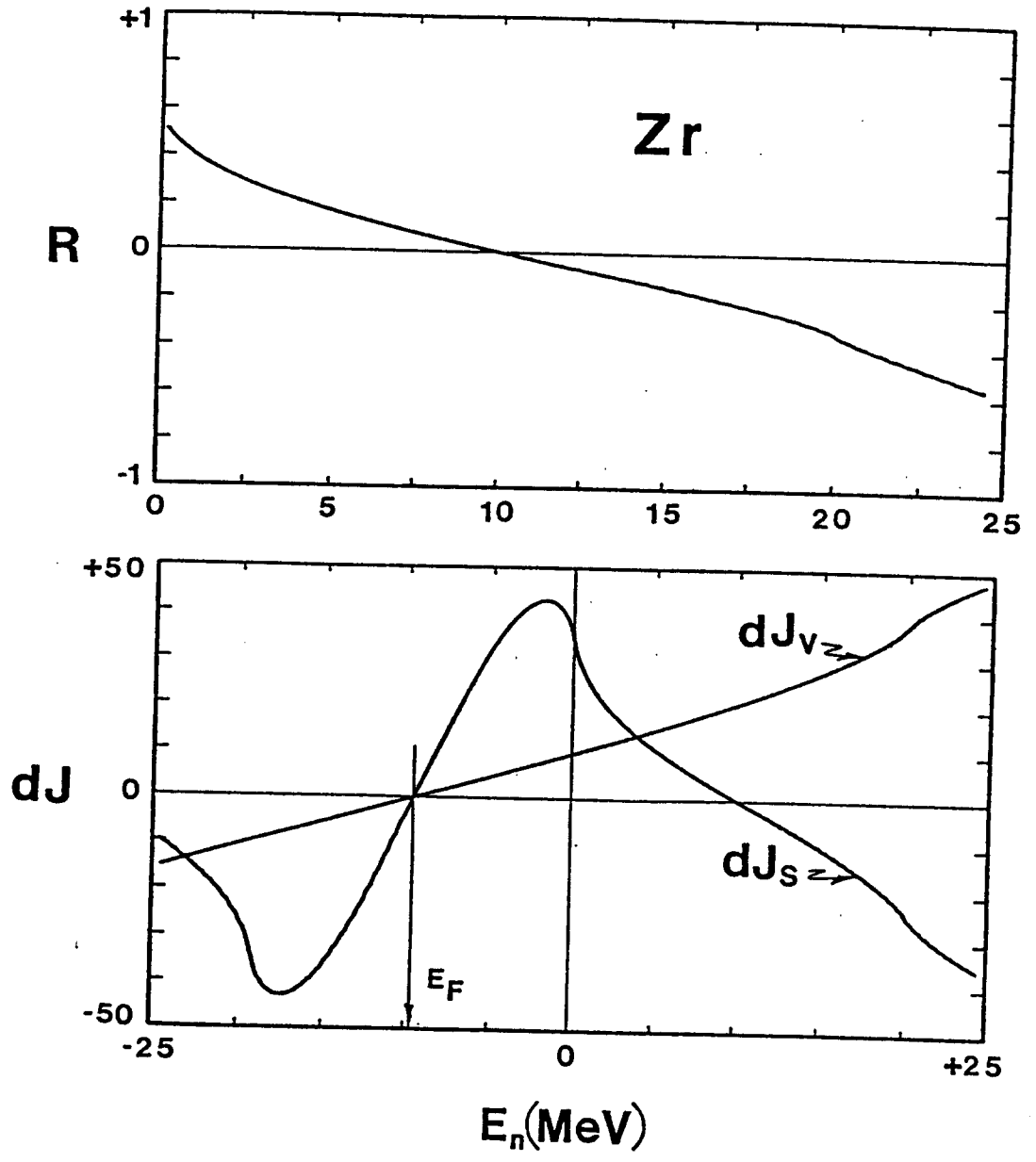

Fig. V–1. The upper portion of the figure shows the R(E) of Eq. V–5, calculated as described in the text. The lower portion of the figure shows the added volume integral per nucleon obtained from the surface (dJ_s) and volume (dJ_v) imaginary potentials (in MeV–fm^3) calculated using Eqs. V–3 and –7.

fitting until self–consistency is obtained. However, the change in $J_s(E)$ is small and one iteration is sufficient. The resulting parameters are listed under the heading DOM (dispersive optical model) in Table V–1. The SOM parameters of the previous section are also given there for comparison. The predictions for the elastic scattering angular distributions and the total cross sections[34] obtained with the DOM parameters are shown in Figs. V–2 and V–3, respectively. It is evident that the calculated results agree very well with experiment. When $(N-Z)/A$ dependencies of the potential strengths, as given in Eqs. IV–11 and –12, are incorporated, the s–and p–wave strength functions deduced by use of the DOM are somewhat different than those given in Table IV–3. However, these differences are only a few percent and, consequently, considerably smaller than the uncertainties associated with the experimentally–deduced values.[36]

From a comparison of the SOM and DOM parameters given in Table V–1, it is clear that the inclusion of the surface real potential barely changes the E–dependence of the geometrical parameters r_v a_v, r_w and a_w. Furthermore, the values of J_s, shown in Fig. V–4, are quite similar to those obtained using the SOM — they increase linearly with energy in the manner defined by the numerical values of Table V–1. On the other hand, J_{eff}, also shown in Fig. V–4, and the J_v of the SOM are quite different, as they should be. Only when dJ_s, Eq. V–3, is added to $J_{eff}(E)$ should the two be compared. In the positive energy range (0 – 25 MeV), $dJ_s(E)$ can be quite well represented as a linear function of energy, i.e.,

$$dJ_s = (25.6 - 2.1 \cdot E) \quad \text{MeV–fm}^3 \, . \tag{V–6}$$

When this expression is added to J_{eff}, a relationship quite similar to that describing J_v is obtained.

Table V–1. Comparison of SOM and DOM optical–model parameters.

	SOM	DOM
Real Pot.		
	$J_v = 471.17 - 5.09 \cdot E$	$J_{eff} = 455.6 - 3.41 \cdot E$ MeV·fm^3
	$r_v = 1.310 - 0.0063 \cdot E$	$= 1.300 - 0.0054 \cdot E$ fm
	$a_v = 0.667$	$= 0.685$ fm
Imaginary Pot.		
	$J_w = 58.36 + 0.74 \cdot E$	$J_s = 60.59 + 0.58 \cdot E$ MeV·fm^3
	$r_w = 1.390 - 0.0063 \cdot E$	$= 1.385 - 0.0071 \cdot E$ fm
	$a_w = 0.310 + 0.0180 \cdot E$	$= 0.255 + 0.0253 \cdot E$ fm

---

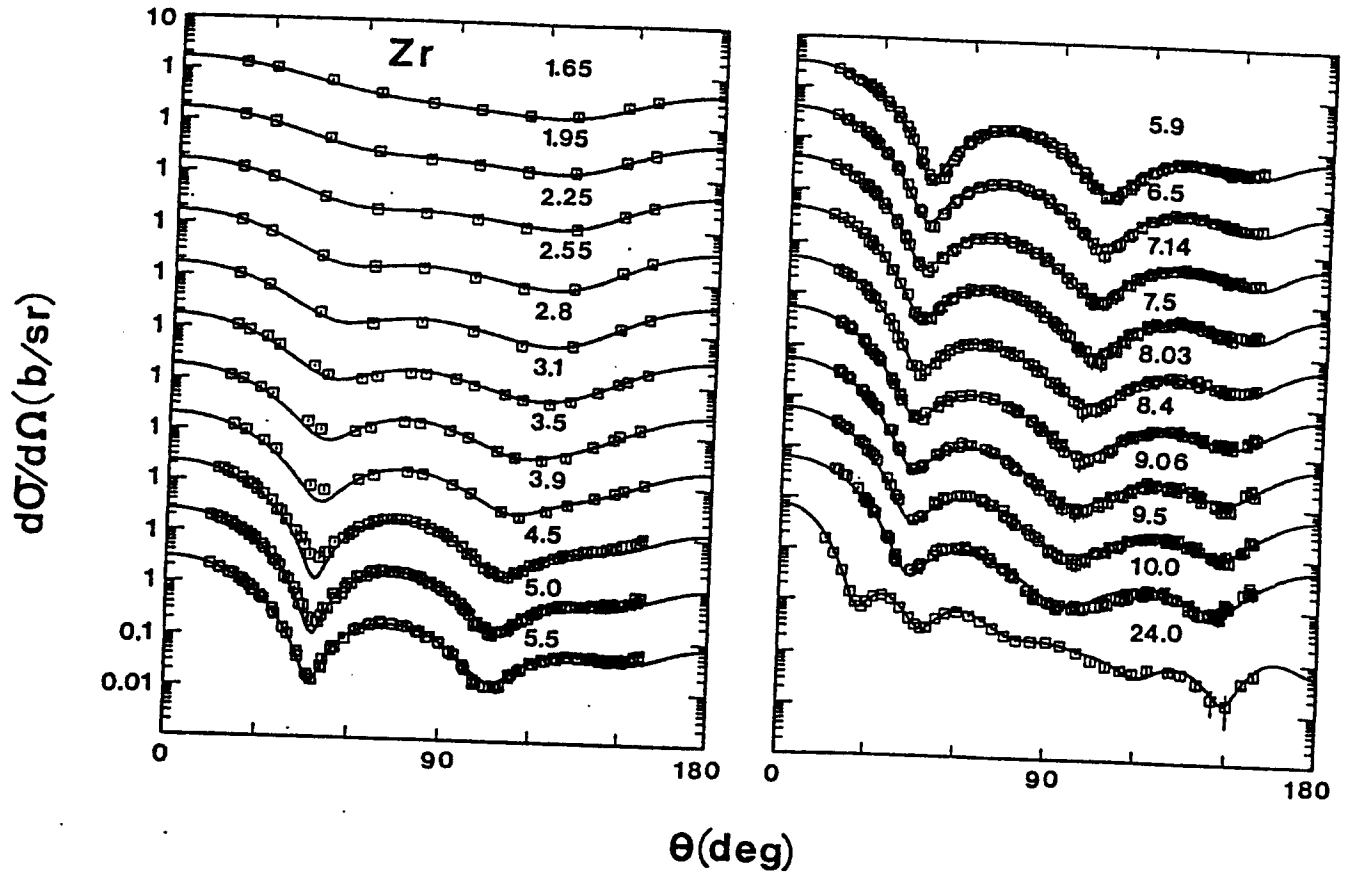

Fig. V–2. Comparison of measured (symbols) and calculated (curves) differential elastic–scattering cross section of elemental zirconium. The calculations were based upon the DOM parameters given in Table V–1. The data are given in the laboratory system.

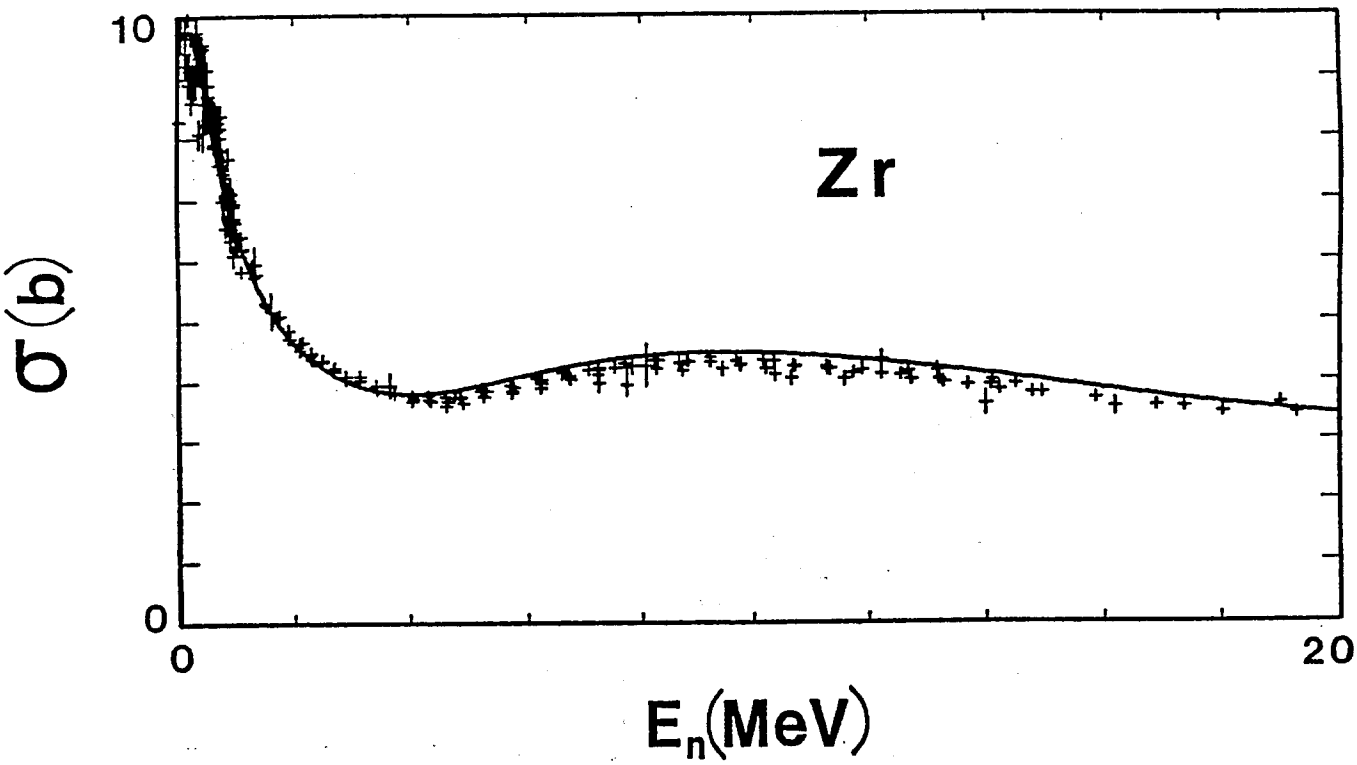

Fig. V–3. Measured (symbols) and calculated (curve) neutron total cross sections of elemental zirconium. The energy–averaged experimental values are taken from the literature as described in ref. 34. The calculations used the DOM parameters of Table V–1.

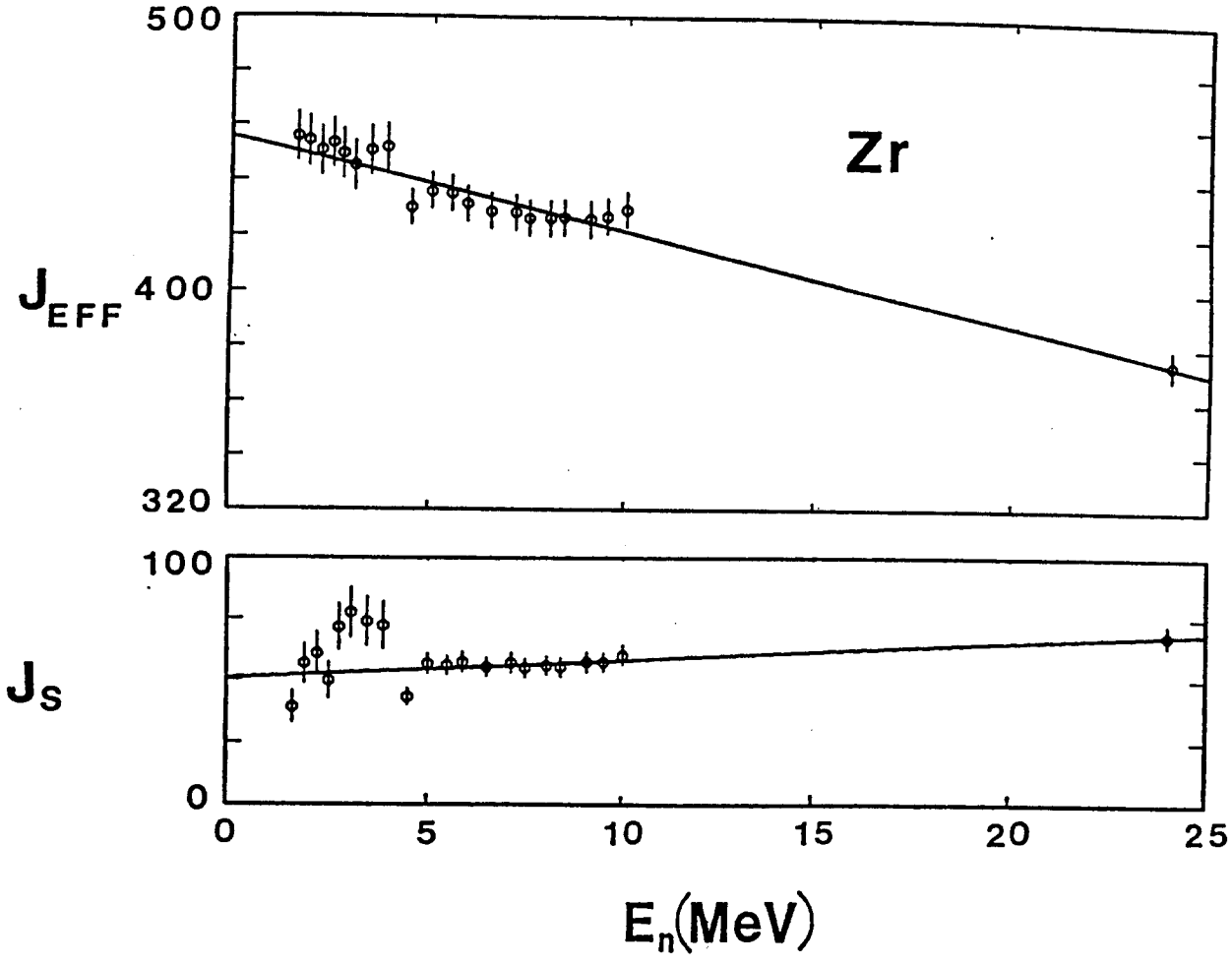

Fig. V–4. Real, J_{eff}, and imaginary, J_s, volume integrals of the potential strengths (in MeV–fm^3) derived from the DOM interpretation of the data. The results of interpretation are indicated by symbols and linear fits to these quantities by curves. The values from the fits are given in Table V–1.

Figure V–5 shows the total real potential, which is the sum of the surface and the volume Woods–Saxon components, as a function of radius at two incident energies, 1 and 24 MeV. From this figure, it is clear that the summed potential is very similar to the simple Woods–Saxon shape.

In the DOM fit to the data, J_{eff}, the sum of the Hartree–Fock component and a possible contribution from volume absorption, can be well represented by a linear function of E, as shown in Fig. V–4. Since $J_{HF}(E)$ is expected to have a simple E dependence, it is important to examine the energy dependence of this added term to be sure that the linear E–dependence of J_{eff} is consistent with this expectation. To estimate the added term, we assume that the volume absorption, which is taken to be symmetric about E_F, is zero for $0 \le E \le E_0$, increases linearly starting at E_0, attains a maximum value of J_m at $E = E_m$, and then is constant for all E greater than E_m. With these assumptions, dJ_v (the volume analog of Eq. V–3), becomes

$$dJ_v(E) = \frac{J_m}{\pi(E_m - E_0)} \left[(E-E_0)\cdot \ln\left|\frac{E_m - E}{E_0 - E}\right| + (E_m - E_0)\cdot \ln\left|\frac{-2E_F + E_m + E}{E_m - E}\right| \right.$$

$$\left. - (-2E_F + E_0 + E)\cdot \ln\left|\frac{-2E_F + E_0 + E}{-2E_F + E_m + E}\right| \right] . \qquad \text{(V–7)}$$

If one, somewhat arbitrarily, takes $E_0 = 25$ MeV (the value of E at which the surface absorption was assumed to begin to decrease), $E_m = 60$ MeV (the value of E at which the surface absorption was assumed to to reach zero) and $J_m = 76.86$ MeV–fm^3 (the peak value of the surface absorption according to Eq. IV–9), then $dJ_v(E)$, as shown in the lower portion of Fig. V–1, will be obtained. As can be seen, $dJ_v(E)$ is small over the entire energy range –25 to +25 MeV, and has an almost linear dependence on E. Thus, the fact that $J_{eff}(E)$ is found experimentally to be a linear function of E is not in conflict with the fact that $J_{HF}(E)$ should be a simple linear function of energy.

The data on J_{eff} (shown in Fig. V–4) were fitted by assuming a linear dependence on bombarding energy. Since J_{eff} is considered to be the sum of Hartree–Fock and volume–absorption contributions, one might attempt to find the strength of this absorption from the measured values by assuming

$$J_{eff}(E) = \alpha + \beta\cdot E + \gamma\cdot dJ_v(E) . \qquad \text{(V–8)}$$

In this expression, the first two terms represent the Hartree–Fock contribution, and the last term is the contribution of the volume absorption. Assuming the simple form of Eq. V–7 for $dJ_v(E)$, the value of γ, and thus the actual volume integral per nucleon of the absorption, can be obtained. Unfortunately, the uncertainties in the data, together with

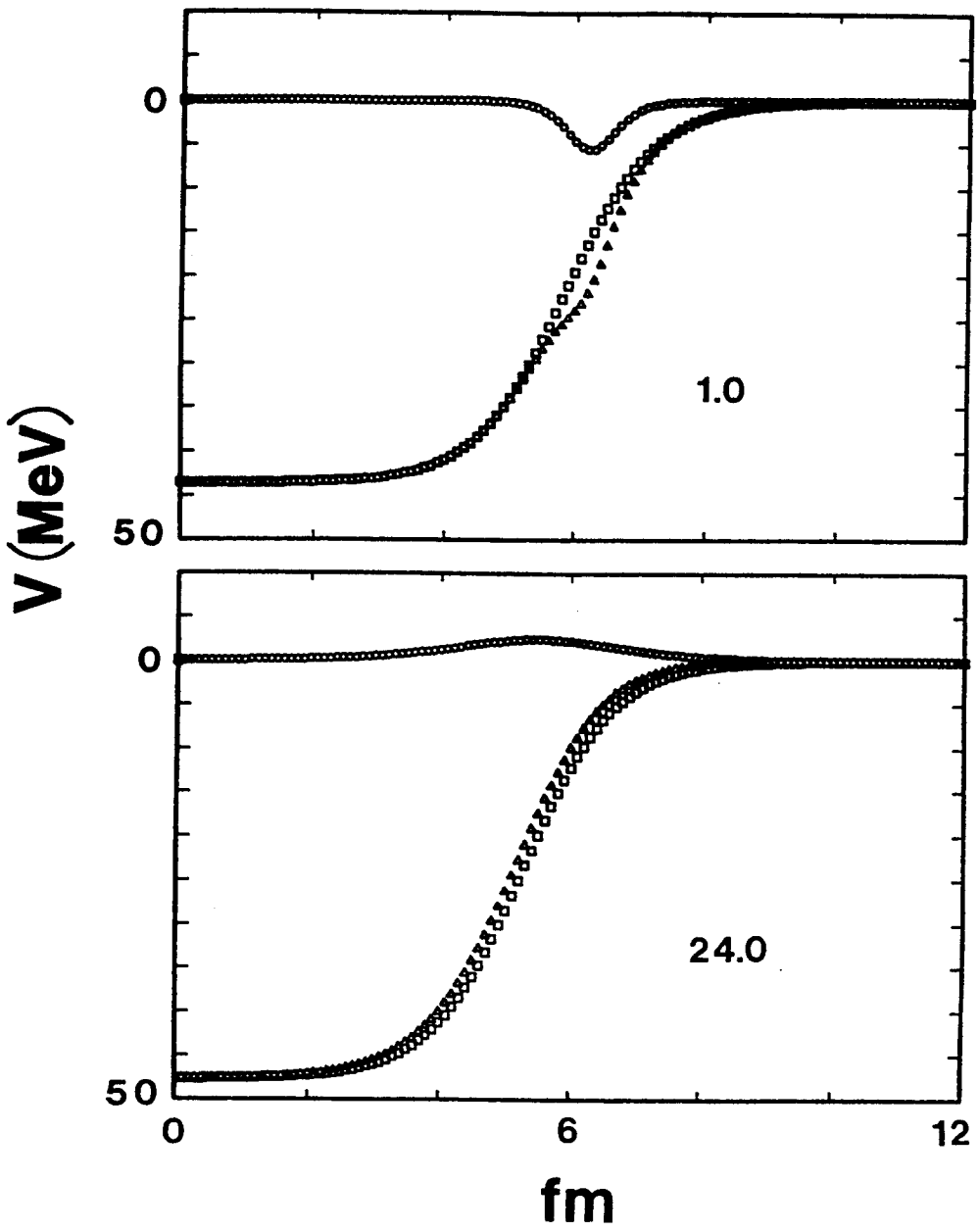

Fig. V–5. DOM real–potential shapes at 1 MeV (upper) and 24 MeV (lower). The effective volume potential is indicated by □ symbols, the surface component by O symbols, and the composite surface plus volume potential by Δ symbols.

the nearly linear energy dependence of $dJ_v(E)$, make this approach impractical. A fit to $J_{eff}(E)$ gives $\gamma = (0.53 \pm 1.76)$.

Although the spin–orbit parameters given in Eq. IV–2 are within the error bars of the values found in the analysis[41] of data on the neighboring nucleus ^{89}Y, the strength of this interaction is somewhat smaller than used in other analyses of data on the separated zirconium isotopes.[5,6] The effect of changing the spin–orbit potential to

$$\begin{aligned} V_{so} &= (6.84 - 0.033 \cdot E) \text{ MeV} \\ r_{so} &= 1.14 \text{ fm} \\ a_{so} &= 0.5 \text{ fm} \end{aligned} \qquad \text{(V–9)}$$

was examined by making a second DOM fit to the data. The parameters resulting from this fit are

$$\begin{aligned} J_{eff} &= (435.94 - 1.46 \cdot E) \text{ MeV–fm}^3 \\ r_v &= (1.2533 - 0.0007 \cdot E) \text{ fm} \\ a_v &= 0.6839 \text{ fm} \\ J_s &= (59.18 + 0.89 \cdot E) \text{ MeV–fm}^3 \\ r_w &= (1.3748 - 0.0048 \cdot E) \text{ fm} \\ a_w &= (0.3419 + 0.0111 \cdot E) \text{ fm.} \end{aligned} \qquad \text{(V–10)}$$

A comparison of these DOM parameters with those of Table V–1 shows that the changes are mainly in the real potential — the energy dependence of r_v has essentially vanished and that of J_{eff} has become quite small. The description of the elastic–scattering distributions is similar to that obtained with the spin–orbit potential of Eq. IV–2. However, as shown in Fig. V–6, the description of the neutron total cross section has markedly deteriorated at energies below several MeV. Thus, a better overall description of the neutron interaction with zirconium is obtained with the DOM of Table V–1 and the spin–orbit potential of Eq. IV–2, and it is suggested that these potentials be used in subsequent DOM analyses of the neutron interaction with the zirconium isotopes.

VI. THE BOUND–STATE POTENTIAL

A. SOM

The dispersion relationship (Eq. V–1) which links the real and imaginary potentials also relates the radial moments of these interactions, i.e.,

$$\langle r(E)^q \rangle_v = \langle r(E)^q \rangle_{HF} + \frac{P}{\pi} \int_{-\infty}^{\infty} \frac{\langle r(E')^q \rangle_w}{E - E'} dE' , \qquad \text{(VI–1)}$$

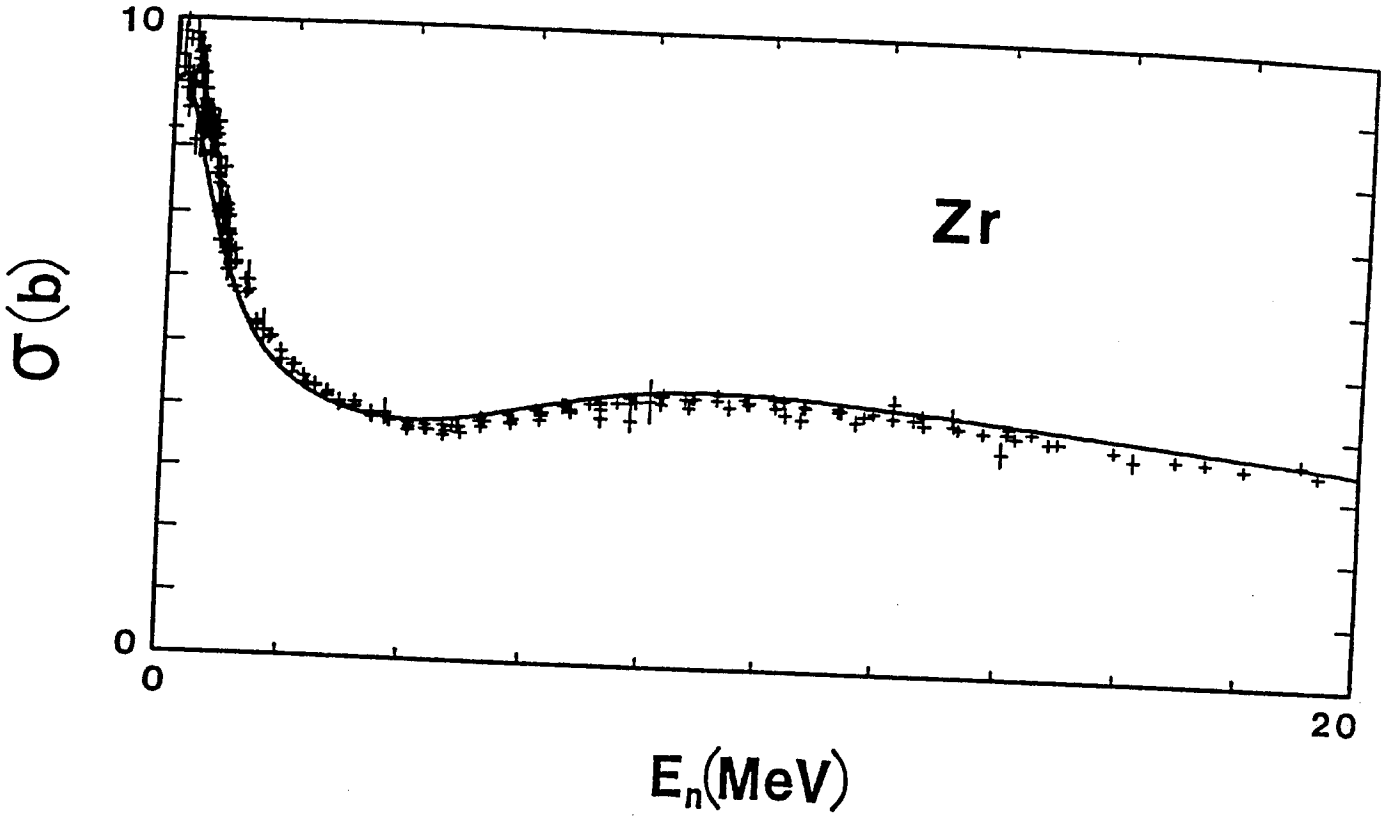

Fig. V–6. Comparison of measured (symbols) and calculated (curve) neutron total cross sections of elemental zirconium. The calculated curve is based upon the DOM of Eqs. V–9 and –10. The notation is identical to that of Fig. V–3.

where, for example,

$$\langle r(E)^q \rangle_w = \frac{4\pi}{A} \int_0^\infty r^q \, W(r,E) dr \, . \qquad \text{(VI–2)}$$

For ^{208}Pb, ^{89}Y, ^{51}V and ^{40}Ca, the $q = 0.8$, 2 and 4 moments of the SOM potential[13,42–45] have been used to investigate the properties of the real interaction implied by Eq. VI–1 when $E < 0$ (i. e., the shell–model potential which is assumed to be a Woods–Saxon well). In these calculations, the Brown–Rho[46] form for the radial moments of the imaginary potential was used,

$$\langle r(E)^q \rangle_w = \frac{C_q (E-E_F)^2}{(E-E_F)^2 + D_q^2} \, , \qquad \text{(VI–3)}$$

so that $\langle r(E)^q \rangle_w$ was assumed to be symmetric about the Fermi energy, E_F. Using the geometry of the imaginary well given by Eqs. IV–5 and –6, together with the 21 values of J_w shown in Fig. IV–1, radial moments for the q values noted above were calculated. The parameters C_q and D_q of Eq. VI–3 were then determined so as to give the best fit to these moments. No assumption was made about the form of the imaginary potential for $E > 24$ MeV, except that, as $E \to \infty$, the various moments approach constant values, C_q, as determined from the fit to the 0 – 24 MeV data.

Because of the simple form assumed for $\langle r(E)^q \rangle_w$, Eq. VI–3, the principal–value integral of Eq. VI–1 can be evaluated analytically. If one assumes that the Hartree–Fock contribution to $\langle r(E)^q \rangle_v$ has, at most, a linear dependence on E, Eq. VI–1 becomes

$$\langle r(E)^q \rangle_v = A_q + B_q \cdot E + \frac{C_q D_q (E-E_F)}{(E-E_F)^2 + D_q^2} \, . \qquad \text{(VI–4)}$$

Using the geometry of the real well given by Eqs. IV–3 and –4, together with the J_v values of Fig. IV–1, the moments of the real potential, $\langle r(E)^q \rangle_v$, were calculated for $q = 0.8$, 2 and 4. With the previously determined C_q and D_q, the A_q and B_q of Eq. VI–4 were determined by least–squares fitting. Values for the various coefficients are given in Table VI–1.

If one assumes that Eq. VI–4 for the three moments of the real potential also applies for negative energies, and if one takes a Woods–Saxon form for the interaction, values of the parameters $V_0(E)$, $r_v(E)$ and $a_v(E)$ needed to characterize the bound–state region, as well as the neutron scattering potential, can be deduced. These are shown as a function energy in Fig. VI–1, together with values of J_v, the volume integral per nucleon of

Table VI–1. Constants Used in Evaluating Eq. VI–4.

Constant	q = 0.8	= 2.0	= 4.0
A_q (MeV·fm^{q+1})	83.64	453.57	11896.0
B_q (fm^{q+1})	–0.523	–4.699	–187.4
C_q (MeV·fm^{q+1})	8.33	70.13	2738.4
D_q (MeV)	5.15	3.9	3.4

Best–fit values for the various moments of the real and imaginary SOM potentials when the parameterizations of Eqs. VI–3 and –4 are used, and E_F = –9.6 MeV.

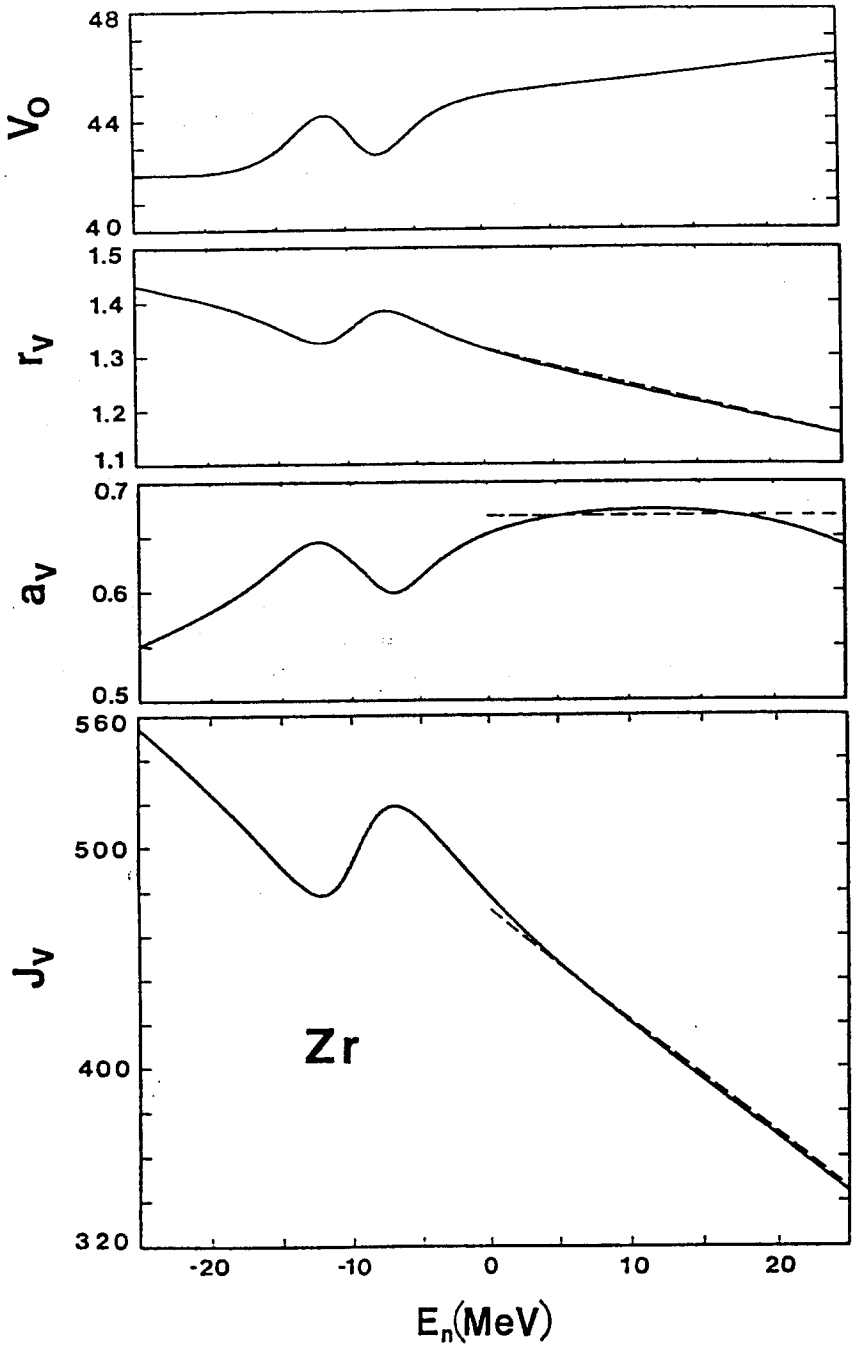

Fig. VI–1. The energy variation of the parameters characterizing the effective Woods–Saxon well deduced using Eq. VI–4 and the parameters of Table VI–1. For positive energies, the values given by a fit to the neutron scattering data are shown as broken lines for r_v (in fm) given by Eq. IV–3, a_v (in fm) by Eq. IV–4, and J_v (in MeV–fm^3) by Eq. IV–12. The strength V_0 is in MeV.

this potential. J_v exhibits the characteristic Fermi Surface Anomaly and, as usual, this occurs at negative energies. The neutron scattering values for r_v, a_v and J_v, given by Eqs. IV–3, –4 and –8, are shown as broken lines in the figure for $E \geq 0$. It is clear that the parameters of the Woods–Saxon potential obtained with the DOM reproduce the positive-energy neutron–scattering results to good accuracy.

If one assumes the shell model spin–orbit strength is given by Eq. IV–2, this can be combined with the values of $V_0(E)$, $r_v(E)$ and $a_v(E)$, shown in Fig. VI–1, to predict the binding energies of the various single particle– and hole–states in ^{90}Zr with the results shown under the "SOM" heading in Fig. VI–2. The figure also displays the comparable experimental data under the heading "EXP". The energies of the $0g_{7/2}$, $1d_{3/2}$, $2s_{1/2}$ and $1d_{5/2}$ particle states were obtained by combining the ^{90}Zr(d,p)^{91}Zr data of Graue et al.[47] with the binding energy tables[48]. From this one concludes that they are bound by 4.4, 4.8, 5.5 and 7.1 MeV, respectively. The $0g_{9/2}$, $1p_{1/2}$, $1p_{3/2}$, $0f_{5/2}$ and $0f_{7/2}$ hole–state energies can be obtained from from the ^{90}Zr($\vec{p}$,d)^{89}Zr results of Kasagi et al.[49]. Their data imply binding energies of 12.1, 13.2, 13.9, 15.2 and 22.3 MeV for these states, respectively. Finally, one would expect the $0h_{11/2}$ level to become bound in this region, and there is evidence for a large number of $\ell = 5$ states in the stripping data. The center of gravity of these states can be calculated from a knowledge of the spectroscopic strength, $\mathscr{S}_i$, to an $\ell = 5$ state at energy E_i, using the relationship

$$\epsilon = \sum_i \mathscr{S}_i E_i / \sum_n \mathscr{S}_n. \qquad \text{(VI–5)}$$

Taking the known values[27] of E_i and $\mathscr{S}_i$, and assuming all the $\ell = 5$ strength has been observed, one concludes that the $0h_{11/2}$ level is bound by about 4.5 MeV.

From a comparison of the SOM and EXP columns in Fig. VI–2, it is clear that there is good agreement for the states with $\ell \leq 2$ — in these cases the rms deviation between theory and experiment is 400 keV. An increase in the spin–orbit force would improve the situation for the $\ell = 4$ and 5 states, provided that the parameters of the Woods–Saxon well, shown in Fig. VI–1, were not appreciably changed. A stronger spin-orbit interaction, which would be consistent with the ^{89}Y results of Honore et al.,[41] would lead to tighter binding of the $0g_{9/2}$ and $0h_{11/2}$ states, would push up the $0g_{7/2}$ state, and would have a minimal effect on the low–spin levels with $\ell \leq 2$. However, because the 0f levels are tightly bound, their calculated values would be less affected by the surface-peaked Thomas term. Thus the $0f_{7/2}$ level would still be too loosely bound, and certainly the $0f_{5/2}$ level would be pushed up. Consequently, a simple increase in the spin–orbit force alone will not be sufficient to reconcile theory and experiment for all bound states.

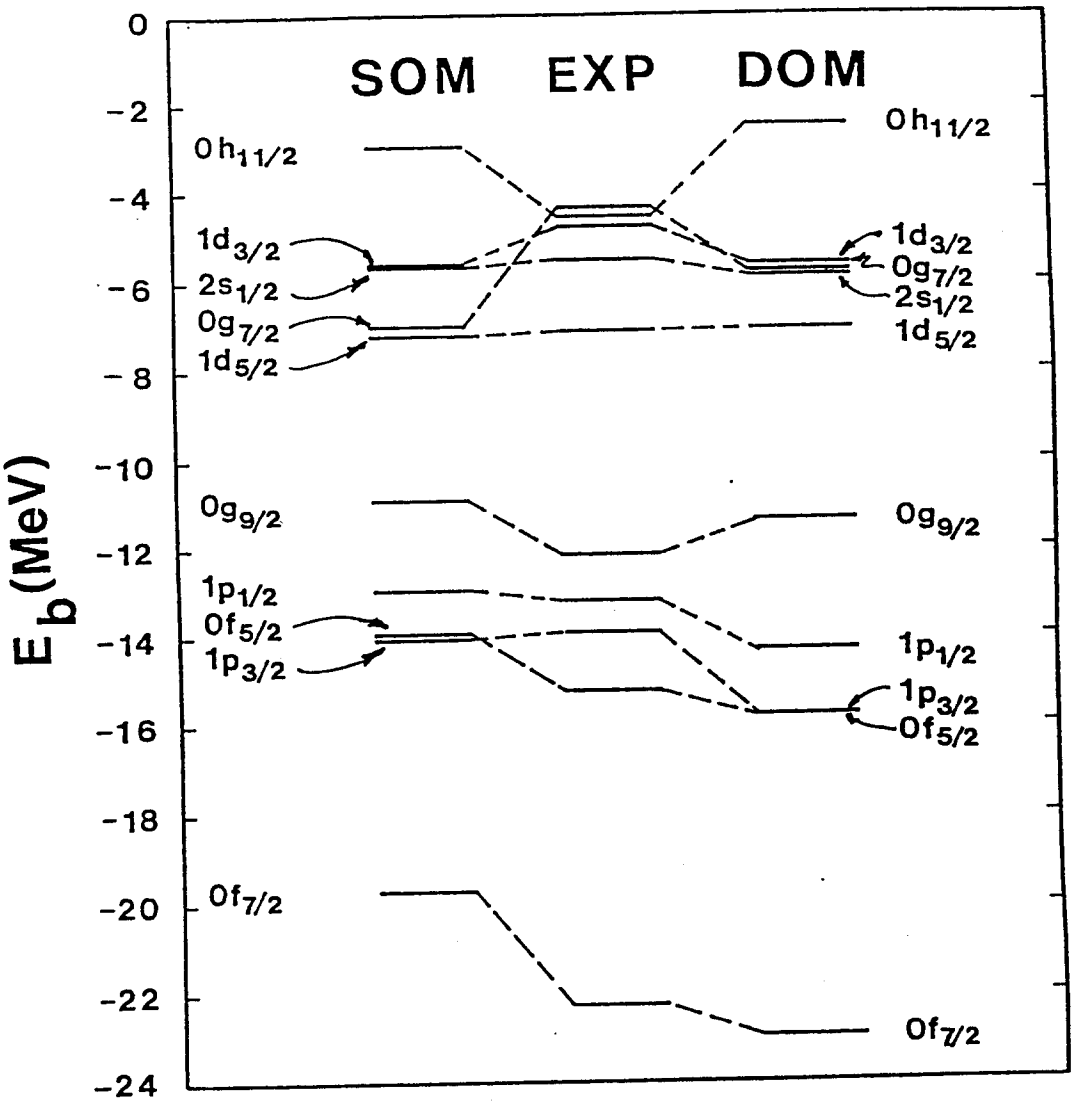

Fig. VI–2. Comparison of experimental (EXP) binding energies (E_b) of the particle– and hole–states in ^{90}Zr with model predictions. The SOM results were obtained with a Woods–Saxon well with the parameters of Fig. VI–1. The DOM results were obtained with the surface–peaked potential added to the Woods–Saxon well as described in the text. In both cases the spin–orbit potential was of the Thomas form with the parameters of Eq. IV–2.

B. DOM

In the DOM analysis of neutron–scattering data, the usual Woods–Saxon real well has added to it a surface term whose strength is given by Eqs. V–3 and V–5. In the bound–state regime we again assume a real surface term whose strength is determined by these equations. In this case, however, the geometry of the well is taken, somewhat arbitrarily, to have the values of a_w and r_w that arise when E = 0. These terms should be added to the real Woods–Saxon well listed under DOM in Table V–1. But, as we shall subsequently discuss, much better agreement with the bound–state data is obtained when the slight E-dependence of r_v is ignored. The results shown in Fig. VI–2, under the column headed DOM, were obtained when the real Woods–Saxon potential for negative energies is given by

$$\begin{aligned} J_v &= (457.7 - 3.41 \cdot E) \quad \text{MeV–fm}^3 \\ r_v &= 1.3 \quad \text{fm} \\ a_v &= 0.685 \quad \text{fm}, \end{aligned} \tag{VI–6}$$

the added real surface potential is a derivative Woods–Saxon form with a strength determined by Eqs. V–3 and –5 with

$$\begin{aligned} r_w &= 1.385 \quad \text{fm} \\ a_w &= 0.255 \quad \text{fm}, \end{aligned} \tag{VI–7}$$

and the spin–orbit interaction has the Thomas form with the parameters of Eq. IV–2. From Fig. VI–2 it is clear that going from the SOM to the DOM changes the s and d states little, provides a distinct improvement for both f and g levels, and slightly degrades the prediction of the $h_{11/2}$ binding energy. On the other hand, the $1p_{1/2}$ and $1p_{3/2}$ binding energies significantly deteriorated, the former now being overbound by 1.1 MeV and the latter by 1.9 MeV. Overall, the general description of particle– and hole–state binding energies is slightly better using the DOM than the SOM; for the former, the rms deviation between theory and experiment is 1.1 MeV, whereas for the latter it is 1.4 MeV.

To use the DOM consistently, one should have taken into account the small energy variation of r_v given in Table V–1. Since the particle states have small values of E, including this E–dependence would have little effect. On the other hand, the continued increase of r_v with increasing binding energy has a devastating effect on the prediction of hole–state binding energies, the rms deviation between theory and experiment is increased from the constant–r_v value of 1.1 MeV to 3.2 MeV! As an alternative, one might assume that r_v has the same E–dependence as given in Table V–1, but is symmetric about the Fermi energy, E_F. If this is done, the rms deviation of the hole states shrinks to 2.1 MeV but still remains much worse than the constant–r_v value.

Thus, it is concluded that our attempt to extrapolate the neutron scattering potential to the bound–state regime meets with only modest success. The energy independent version of the DOM provides a significantly better picture of the bound–state

data than do the two energy–dependent versions discussed, and it is also slightly better at describing the experimental results than is the SOM.

VII. SUMMARY DISCUSSION

When the spin–orbit interaction of Eq. IV–2 is combined with the SOM or DOM parameters given in Table V–1, a good description of both the elemental zirconium differential elastic scattering and neutron total cross sections between $\approx < 1$ and 24 MeV is obtained. From Table V–1 it is evident that the volume–integral–per–nucleon of the DOM real potential is smaller in magnitude and less energy dependent than its SOM counterpart. This is consistent with the fact that the added surface component, dJ_s, has the same sign and energy slope as J_{eff} (see Eq. V–6). Thus, although dJ_s is only about 5% of the total J_v, it appears that about 30% of the E–dependence of J_v in the conventional SOM is due to the dispersive–integral contribution. It is also clear from Fig. V–5 that the use of the DOM should decrease the energy dependence of r_v relative to that of the SOM, and indeed this is true. However, a small but significant dependence of r_v remains when the DOM is used. Finally, for both models, a_v is energy independent, and its SOM and DOM values differ by a small amount that is probably not significant.

In a recent paper,[50] the dependence of the SOM r_v and J_v on mass number was studied at 8 MeV. Over the range A = 51 to 209, it was found that both r_v and J_v decrease with increasing A. The 8 MeV values found in the present SOM interpretation fit nicely into the systematics of Ref. 50, and, moreover, the present a_v is nearly identical to the average value, 0.67 fm, found for the A = 51 to 209 nuclei. Since the SOM real potential is the sum of a smooth Hartree–Fock term and a nucleus–dependent dispersion contribution, one might have expected a deviation from the smooth A dependence. However, as already noted, the dispersion–integral contribution is only about 5% of J_v, and also at 8 MeV dJ_s is almost zero.

Turning to the imaginary potential, one sees from Table V–1 that, for both the SOM and the DOM, r_w decreases with increasing energy, whereas a_w increases. This behavior already has been noted in our analysis of the neutron–scattering data for other nuclei[44,50–54] (^{51}V, ^{58}Ni, ^{59}Co, ^{89}Y, ^{115}In and ^{209}Bi). As expected, J_w increases with energy, since at higher energies more inelastic channels are open. Up to 24 MeV, we find no evidence for volume absorption, and this is consistent with the findings of Wang and Rapaport[6] who studied the 24–MeV scattering from separated Zr isotopes. From our work on elemental zirconium, we can say nothing about the isotopic behavior of the potential. However, from the work of Wang and Rapaport[6] it is clear that J_w increases with increasing $(N - Z)/A$ (see Eq. IV–12). This result has been found for other nuclei near closed shells,[10] and it reflects the fact that at closed shells the number of open channels is at a minimum. This finding is contrary to the $(N - Z)/A$ dependence of J_w proposed in

global models,[7,8] and it again points up the fact that the imaginary potential is nuclear–structure dependent. Thus, although a global model is probably adequate for the real potential, it certainly is not for the imaginary interaction. At the very least, a local model should be employed for the imaginary potential.

When the $(N - Z)/A$ dependence of the potentials, given by Eqs. IV–11 and –12, is invoked, our model describes quite well the elastic scattering from the various Zr isotopes (see Figs. IV–4 and –5). At low energies, compound–nucleus inelastic scattering to individual levels is predicted to be fairly large, and this agrees reasonably well with the elemental and isotopic experimental data (see Figs. III–2, IV–6 and IV–7). At higher energies, our experimental resolution (in the context of the elemental complexity) limits our inelastic–scattering results to groups consisting of contributions from several isotopes. Inelastic scattering to both the $1.85 - 2.2$ MeV and $2.6 - 2.9$ MeV groups is predicted to be $\approx > 100$ mb, on the basis of compound nucleus theory, and this is in fair agreement with experiment. On the other hand, the predicted compound–nucleus cross section for the excitation of the "941 keV level" is much smaller than observed, clearly indicating a large direct–reaction component. Its required magnitude is about the same as that found by Wang and Rapaport[6] for scattering to the yrast 2^+ states in ^{92}Zr and ^{94}Zr.

The real optical–model potentials have been extrapolated to negative energies, and the predicted binding energies of single–particle and –hole states of ^{90}Zr are compared with experiment in Fig. VI–2. For the SOM this potential was assumed to have a Woods-Saxon form, with the parameters shown in Fig. VI–1. In this case, the rms deviation between theory and experiment is 1.4 MeV for the particle states, and the same magnitude was found for the hole states. For the DOM, the shell model potential is a sum of two terms: a Woods–Saxon well with the parameters of Eq. VI–6, plus a derivative Woods-Saxon contribution with a geometry given by Eq. VI–7 and a strength determined by the dispersion integral (Eqs. V–3 to V–5). The DOM description of the binding energies is somewhat better than obtained with the SOM model; the rms deviation of the particle states is 1.2 MeV, and the hole states 1.1 MeV. Delaroche, Wang and Rapaport[5] have also studied the bound–state problem using a DOM determined from a fit to their ^{90}Zr data. With their model interaction, the predicted particle states are somewhat closer to experiment — the rms deviation is 0.8 MeV. On the other hand, their predicted hole states have an rms deviation of 2 MeV.

In determining the binding energies of the ^{90}Zr states, it was assumed that all the stripping and pickup strength had been observed. Any missed stripping strength would imply looser binding for the particle states, and any missed pickup strength would lead to tighter hole–state binding. With the exception of the $0h_{11/2}$ level, both our calculation and that of Delaroche et al.[5] predict particle states to be more tightly bound than experiment. Thus, except for the $0h_{11/2}$, any missed stripping strength would worsen the agreement between theory and experiment for the particle states. On the other hand, with the exception of the $0g_{9/2}$ state, all hole states are predicted to be too tightly bound on the basis of both our DOM and that of Delaroche et al. Thus missed pickup strength would improve the agreement between theory and experiment for all the hole states, except the $0g_{9/2}$. For the SOM, shown in Fig. VI–2, only the $1p_{3/2}$ state is predicted to be too tightly bound, so for this model missed pickup strength would worsen the agreement between theory and experiment. Thus it would appear that, even with the optimum

scenario on missed stripping and pickup strengths, the extrapolation of the ^{90}Zr scattering potential to the bound–state regime leads to predictions for binding energies that are considerably worse than were obtained, for example, from a similar extrapolation[44] in ^{51}V. In this latter case, the rms deviation between theory and experiment for the particle states was 550 keV, and for the hole states 700 keV.

The data[41] on the neighboring nucleus, ^{89}Y, indicates that the spin–orbit strength may be slightly larger than given by Eq. IV–2, and indeed two recent analyses[5,6] of zirconium data have used a larger value for this interaction. Although the values of the spin–orbit parameters (Eq. IV–2) are within the uncertainties given in the ^{89}Y analysis, we have redone the DOM interpretation using the strength, Eq. V–9, determined from studies of this neighboring nucleus.[41] The resulting best–fit parameters of the real Woods–Saxon and imaginary derivative Woods–Saxon wells are given in Eq. V–10. The low–energy neutron total cross sections predicted by this model are substantially smaller than experiment (see Fig. V–6). This shortcoming is mainly due to the small value of r_v at low energies in this model. Models based upon low–energy data, for example that of Moldauer[55], generally lead to r_v values in the neighborhood of 1.3 fm. When the potentials described by Eqs. V–9 and –10 are extrapolated to the bound region, and E = 0 values are used for V_{so}, r_v, r_w and a_w, all states except the $1p_{3/2}$ are predicted to be less tightly bound than experiment because of the very slow increase in J_v with decreasing energy. This actually lowers the rms deviation between theory and experiment for the particle states to 0.8 MeV, but worsens the predictions for the hole states to an rms deviation of 1.7 MeV. Thus, if Zr data are analyzed using the DOM the parameters of Table V–1 and the spin–orbit strength of Eq. IV–2 should be used.

Finally, most of the parameters of the above SOM and DOM exhibit energy dependencies that are reasonably represented by linear expressions. These are clearly first approximations, valid only over the energy range of the present interpretations. They should not be used to extrapolate to far higher energies. It is reasonable to expect that energy–independent values are asymptotically approached above 20 to 25 MeV. This transition may already be under way between 10 and 24 MeV, but it is impossible to tell due to absence of experimental information in this energy region. For the calculation of neutron properties for applied purposes, the SOM of this work should be quite suitable to $\approx$ 25 MeV; i.e., over the energy range of primary applied interest. The introduction of the additional complexities of the DOM will mitigate some of the energy dependencies of the SOM parameters, but will not entirely remove them. Thus the use of the DOM is probably not warranted for engineering applications; rather, its main value is in the fundamental understanding of structure and the neutron interaction with the zirconium nuclei.

REFERENCES

1. P. E. Hodgson Nuclear Reactions and Nuclear Structure (Clarendon, Oxford, 1971).
2. G. R. Satchler Direct Nuclear Reactions (Clarendon, Oxford, 1983).
3. C. E. Till and Y. I. Chang, Advances in Nucl. Sci. and Technology, 20 127 (1988).
4. A. M. Lane, Phys. Rev. Lett. 8 171 (1962).
5. J. P. Delaroche, Y. Wang and J. Rapaport, Phys. Rev. C39 391 (1989).
6. Y. Wang and J. Rapaport, Nucl. Phys. A517 301 (1990).
7. R. L. Walter and P. P. Guss, Proc. Conf. Nucl. Data for Basic and Applied Science, vol.–2, p.–1079, Gordon and Breach, New York (1986).
8. J. Rapaport, Phys. Reports 87 25 (1982).
9. R. D. Lawson, P. T. Guenther and A. B. Smith, Nucl. Phys. A519 487 (1990).
10. A. M. Lane, J. E. Lynn, E. Melkonian and E. Rae, Phys. Rev. Lett. 2 424 (1959); W. Vonach, A. B. Smith and P. A. Moldauer, Phys. Lett. 11 331 (1964).
11. P. E. Hodgson, private communication.
12. C. Mahaux and H. Ngo, Phys. Lett. 100B 285 (1981); Nucl. Phys. A378 205 (1982).
13. C. Mahaux and R. Sartor, Phys. Rev. Lett. 57 3015 (1986).
14. C. Mahaux and R. Sartor, in Advances in Nuclear Physics edited by J. W. Negele and Erich Vogt, Plenum Press, New York, to be published.
15. A. Smith, P. Guenther, R. Larson, C. Nelson, P. Walker and J. Whalen, Nucl. Instr. Methods, 50 277 (1967).
16. C. Budtz–Jorgensen, P. Guenther, A. Smith, J. Whalen, W. McMurray, M. Renan and I. Van Heerden, Z. Phys., A319 47 (1984).
17. S. Chiba, P. T. Guenther and A. B. Smith, Argonne National Laboratory Report, ANL/NDM–112 (1990).
18. M. Drosg, IAEA–TECDOC–410, 239, IAEA Press, Vienna (1987).
19. NE–213 scintillator, Nuclear Enterprises, Ltd., Edinburgh.
20. A. Smith, P. Guenther and R. Sjoblum, Nucl. Instr. Methods, 140 397 (1977).
21. H. Conde, A. Smith and A. Lorenz, eds., Nuclear standards file, IAEA Tech Report 227, IAEA Press, Vienna (1983).
22. A. B. Smith, P. T. Guenther and R. D. McKnight, Proc. Conf. Nucl. Data for Sci. and Technology, page–39, R. Reidel Pub. Co., Dordrecht, Holland (1982).

23. P. T. Guenther, Elastic and inelastic neutron scattering from the even isotopes of tungsten, Univ. of Illinois Thesis (1977).

24. A. B. Smith, MONTE–SPHERE and MONTE–POLY, Monte–Carlo corrections codes, Unpublished memoranda (1988), available from the author.

25. A. B. Smith and P. T. Guenther, Argonne National Laboratory Report, ANL/NDM–69 (1982).

26. D. C. Kocher, Nucl. Data Sheets, 16 55 (1975).

27. H. W. Muller, Nucl. Data Sheets, 31 181 (1980) and 60 835 (1990).

28. P. Luksch, Nucl. Data Sheets 30 573 (1980).

29. H. W. Muller, Nucl. Data Sheets, 44 277 (1985).

30. Chart of the Nuclides 13^{th} Edition, F. W. Walker, D. G. Miller and F. Feiner, General Electric Co. (1983).

31. P. A. Moldauer, private communication (1982); as modified by S. Chiba (1989).

32. W. Hauser and H. Feshbach, Phys. Rev. 87 366 (1952).

33. P. A. Moldauer, Nucl. Phys. A344 185 (1980).

34. S. Chiba, P. T. Guenther, J. W. Meadows, R. D. Lawson, A. B. Smith, D. L. Smith and R. J. Howerton, Argonne National Lab. Report, to be published.

35. A. Gilbert and A. Cameron, Can. J. Phys. 43 1446 (1965).

36. S. F. Mughabghab, M. Divadeenam and N. E. Holden, Neutron Cross Sections Academic Press, New York (1981).

37. S. Tanaka, EXFOR21638002, Data available at the National Nuclear Data Center, Brookhaven National Laboratory.

38. R. W. Stooksberry, J. H. Anderson and M. Goldsmith, Phys. Rev. C13 1061 (1976).

39. F. D. McDaniel, J. D. Brandenberger, G. D. Glasgow and H. G. Leighton, Phys. Rev. C10 1087 (1974).

40. A. B. Smith, A Monte–Carlo time of flight simulation code, unpublished memorandum (1990), available from the author.

41. G. M. Honore, R. S. Pedroni, C. R. Howell, H. G. Pfutzner, R. C. Byrd, G. Tungate and R. L. Walter, Phys. Rev. C34 825 (1986).

42. C. Mahaux and R. Sartor, Nucl. Phys. A468 193 (1987).

43. C. Mahaux and R. Sartor, Phys. Rev. C36 1777 (1987).

44. R. D. Lawson, P. T. Guenther and A. B. Smith, Nucl. Phys. A493 267 (1989).

45. C. Mahaux and R. Sartor, Nucl. Phys. A484 205 (1988).

46. G. E. Brown and M. Rho, Nucl. Phys. A372 397 (1981).

47. A. Graue, L. H. Herland, K. J. Lervik, J. T. Nesse and E. R. Cosman, Nucl. Phys. A187 141 (1972).

48. A. H. Wapstra and K. Bos, At. Data and Nucl Data Tables 19 177 (1977).

49. J. Kasagi, G. M. Crawley, E. Kashy, J. Duffy, S. Gales, E. Gerlic and D. Friesel, Phys. Rev. C28 1065 (1983).

50. S. Chiba, P. T. Guenther, R. D. Lawson and A. B. Smith, Phys. Rev. C42 2487 (1990).

51. A. B. Smith et al., to be published.

52. A. B. Smith, P. T. Guenther and R. D. Lawson, Nucl. Phys. A483 50 (1988).

53. R. D. Lawson, P. T. Guenther and A. B. Smith, Phys. Rev. C34 1599 (1986).

54. R. D. Lawson, P. T. Guenther and A. B. Smith, Phys. Rev. C36 1298 (1987).

55. P. A. Moldauer, Nucl. Phys. 47 65 (1963).